Low Temperature Creep/Relaxation Behaviour of PM Steels under Static Load

by

MAHESWARAN VATTUR SUNDARAM

Diploma work No. 121/2013
at Department of Materials and Manufacturing Technology
CHALMERS UNIVERSITY OF TECHNOLOGY
Gothenburg, Sweden

Diploma work in the Master programme Materials Engineering

Performed at: Department of Materials and Manufacturing Technology
Chalmers University of Technology
SE-412 96 Gothenburg

Supervisor: Kumar Babu Surreddi, PhD
Department of Materials and Manufacturing Technology
Chalmers University of Technology
SE-412 96 Gothenburg

Industrial Supervisor: Henrik Karlsson, PhD
Materials Technology
Volvo Group Trucks Technology
SE-405 08 Gothenburg

Examiner & Supervisor : Assoc. Prof. Eduard Hryha, PhD
Department of Materials and Manufacturing Technology
Chalmers University of Technology
SE-412 96 Gothenburg

Low Temperature Creep/Relaxation Behaviour of PM Steels under Static Load

MAHESWARAN VATTUR SUNDARAM

Diploma work no 121/2013
Department of Materials and Manufacturing Technology
Chalmers University of Technology
SE-412 96 Gothenburg
Sweden
Telephone + 46 (0)31-772 1000

Cover: SEM image of the fractured PM component, showing transparticle dimple ductile fracture

Chalmers Reproservice
Gothenburg, Sweden 2013

கற்றது கைமண் அளவு,
கல்லாதது உலகளவு

- ஔவையார்

What we have learned
Is like a handful of earth;
What we have yet to learn
Is like the whole world

- Auvaiyar, 4th Century Tamil poet

Low Temperature Creep/Relaxation Behaviour of PM Steels under Static Load

MAHESWARAN VATTUR SUNDARAM
Department of Materials and Manufacturing Technology
Chalmers University of Technology

Abstract

Powder metallurgy (PM) is one of the metal forming techniques to manufacture structural components in high volumes. Almost 70% of the PM steels produced are used in automotive applications. This is due to the inherent advantages of the PM process owing to its low cost and near net shaping capabilities along with the possibility of achieving complex shapes while utilizing almost 95% of the raw material with less energy consumption. Utilizing PM components for high performance applications demands good mechanical properties and high dimensional tolerances. In PM steels such properties are achieved, for example by modifying the composition (alloying elements), utilizing different alloying techniques (prealloying, diffusion bonding and admixing) and application of heat treatments (e.g. hardening/sinterhardening, carburising, tempering, etc.).

It has recently been found that under certain conditions, PM steel components lack dimensional stability in applications under high static loads over a sustained period of time at temperatures where creep normally doesn't occur. In high performance applications, such a small dimensional instability could have an adverse effect on the overall performance of the system. Preliminary tests indicate that the components tend to creep/relax at low temperatures under high loading conditions. This phenomenon is a recent observation in PM steels, whereas, in bearing steels and other metallic materials (i.e. Cu, Ti) such behaviour has been discussed earlier.

Hence, the creep/relaxation phenomena at temperatures (T/T_m<0.3, temperature in kelvin) in PM steels under high static loading conditions is investigated for diffusion-alloyed powder grade (Distaloy HP produced by Höganäs AB) material. The experiments were performed on the sinterhardened tensile specimens that were additionally heat treated as follows: (i) without any tempering (untempered); (ii) after subsequent tempering at 200°C and 300°C (tempered); (iii) specimens with subsequent quenching in liquid nitrogen directly after sinterhardening (untempered-deep cooled); (iv) sinterhardened and quenched in liquid nitrogen specimens with subsequent tempering at 200°C and 300°C (deepcooled-tempered). The test specimens are characterised and the properties are analysed and evaluated before and after creep tests by XRD, optical and scanning electron microscopy.

The results show that each specimen exhibits a unique characteristic behaviour associated with the test temperature and corresponding tempering conditions. However, untempered specimens exhibited a noticeable amount of plastic strain at 120°C when compared to the tempered (at 200°C) specimens. For the specimens tempered at a higher temperature (at 300°C) there is a negligible amount of plastic strain when testing under similar conditions. Also, the deepcooled-tempered specimens exhibited smaller amount of strain when compared to the only tempered samples. This behaviour of the specimens is attributed to the microstructural stability and stress relieve while tempering at high temperatures reduces the dimensional instability of the above studied PM steel under high static loads over a prolonged time period. A more detailed study for understanding this phenomenon in PM steels is required to further widen their application in automotive industry.

Keywords: *diffusion alloyed PM steels, sinterhardening, tempering, low temperature creep/relaxation, dimensional stability.*

Preface

This work has been performed as a Master thesis work at the Department of Materials and Manufacturing technology, Chalmers University of Technology (Gothenburg, Sweden).

This project is in cooperation between Chalmers, Volvo Group Trucks Technology and Höganäs AB and funded by Swedish Agency for Innovation Systems (VINNOVA) within the framework of the Swedish Automotive Research agenda.

During this time period, one paper was published and one is in manuscript:

- K.B. Surreddi, M. Vattur Sundaram, E. Hryha, H. Karlsson, M. Andersson, L. Nyborg: **"Low Temperature Creep Behavior of PM Components Under Static Load Conditions",** in *Euro PM2013 Proceedings-Sintered Steels.-.Tailored Mechanical Properties,* 2013, vol.3, pp. 349-354
- M. Vattur Sundaram, K.B. Surreddi, E. Hryha, H. Karlsson, M. Andersson, L. Nyborg: **"Investigation of Low Temperature Creep Behaviour of PM steels",** *In manuscript*

Contents

1 Introduction

1.1 Background

In recent observations, it has been found that the PM steel components when used under high static loads experience a dimensional change. This behaviour is reported in case of components subjected to high static loads over a period of time at low temperature ranges (100-150°C). In high performance applications even a small dimensional change could have an adverse effect on the overall performance of the system. Initial investigations performed on components indicate that they tend to creep/relax under static loads over a sustained time period at a temperature of around 120°C, where creep normally does not occur for these types of materials. Based on the preliminary test results, a hypothesis concerning low-temperature creep is postulated aiming to predict the dimensional stability behaviour at low temperatures at a lab scale.

There is no literature or previous investigations concerning low temperature creep of PM steels. Some studies have been performed regarding the low temperature creep in case of bearing steels [1]–[3], some mild and high-strength steels and pure metals such as copper and titanium [4]–[10]. When, considering PM steels, the additional factors influencing the performance of the component would be porosity and interparticle necks which determine the strength of the component. Combination of all these parameters makes it more complicated to determine the actual mechanism behind this phenomenon.

1.2 Objective

The objective of this work is to perform a detailed investigation of low temperature creep/relaxation behaviour on standard tensile specimens prepared from a diffusion alloyed powder grade Distaloy HP. The samples are processed in a similar route as that of the actual components. The scope of the thesis is:

- To simulate creep/relaxation of PM components at a lab scale by experimenting on the standard tensile specimens to observe creep/relaxation under loading conditions around 90% of the yield strength of the material and at temperatures $T/T_m < 0.3$
- To identify possible microstructural changes taking place during creep tests by investigation of the specimens before and after creep testing using metallurgical characterisation techniques
- To build a theoretical model and identify the physical phenomena behind the low temperature creep behaviour in PM steels
- To propose appropriate components' treatment to avoid or minimize creep/relaxation behaviour during use.

2 Theoretical Background

2.1 Powder Metallurgy Introduction

Powder Metallurgy (PM) is a cost effective technique for manufacturing of structural steel components with complex geometry and tailored properties utilizing 95% of the raw material with very low energy consumption compared to other manufacturing techniques (e.g. machining, forging and casting). The proof of ancient use of powder metallurgical manufacturing references back to standing evidence of Delhi iron pillar, India. Use of gold powder in jewellery by Incas was also found. Modern powder metallurgy began in the beginning of the 20th century and several technological advancements have taken place during the last century [11]–[14].

As of 2012, an average North American vehicle contains 20 kg of PM parts and corresponding European vehicle contains 8.8 kg and in case of Japanese vehicle it declined by 0.3 kg to 9.1 kg of PM parts. However, the North American automotive base engine contains ~30% of parts made by PM technique. In terms of base engine components, the low demanding (in terms of performance) parts are identified and the potential could be to convert into PM for high demanding engine and transmission components [15], [16] and also parts for other applications such as in commercial vehicles. For heavy duty engines, the demand for large and stable structural parts with very high strength arises, where the stability of the components and ability to withstand high loads are of the main concern. This can be achieved either by making relatively high density components or sintered parts with appropriate alloying additions and methods (prealloying, diffusion bonding, etc.) as well as applying heat treatment operations.

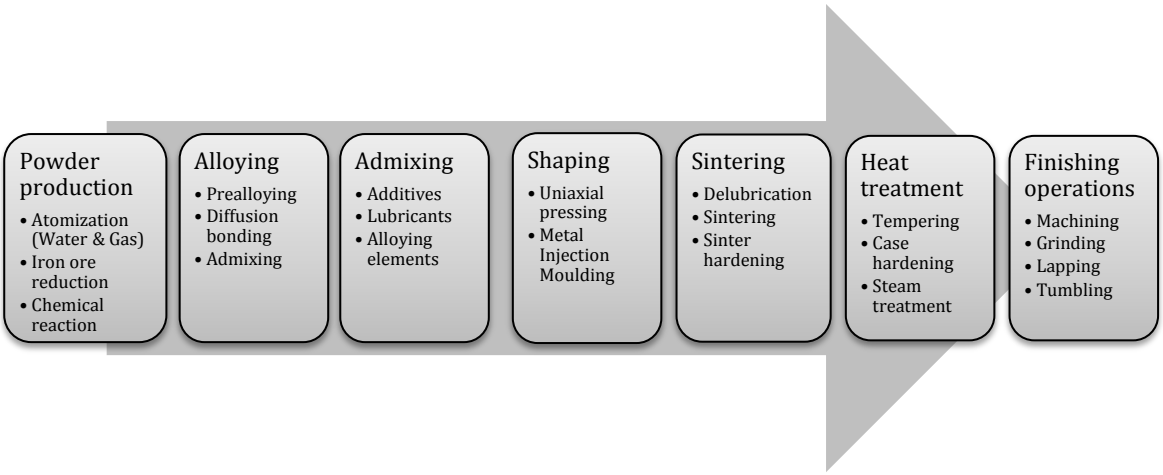

Figure 1 : A typical processing route for PM Components manufacturing

Figure 1 shows a typical processing route for PM components. Due to high interdependency between different segments in the PM process, variations in process parameters in one segment will have an impact on the final properties. Owing to the high number of variants in processing, controlling the product outcome is challenging. There are variations in each segment of the individual parameters that affects the final performance as discussed by Bergquist [17]. Thus control over the process in each stage determines the product performance.

2.1.1 Powder Production

Iron powder accounts for almost 80% of the overall powder production. With the increase in use of PM steels, a number of powder grades were developed in recent times due to the increasing demand for high performance applications. Iron and steel powders for PM steels are produced mainly by the following processes [11], [18]

- Atomization (water and gas)
- Sponge iron reduction
- Chemical reaction

In case of structural components for automotive industry, powder is mainly produced by water atomization which will be discussed in detail in the following section. In few cases, sponge iron powder is also used as a base material.

2.1.1.1 Water atomization

High pressure water jets are injected onto a stream of molten metal in order to disintegrate into tiny droplets (Figure 2) which solidify rapidly, forming irregularly shaped powder particles, as shown in Figure 3. Water pressure is a critical controlling parameter for the process, as it determines the particle size and the cooling rate (which is usually in the range of 10^4-10^8 K/s). Water atomization is a low-cost technique for high volume iron powder production [11], [18].

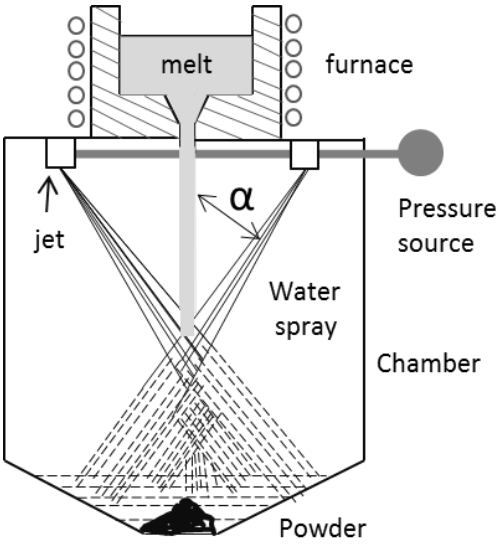

Figure 2 : Water atomization illustration redrawn from [11]

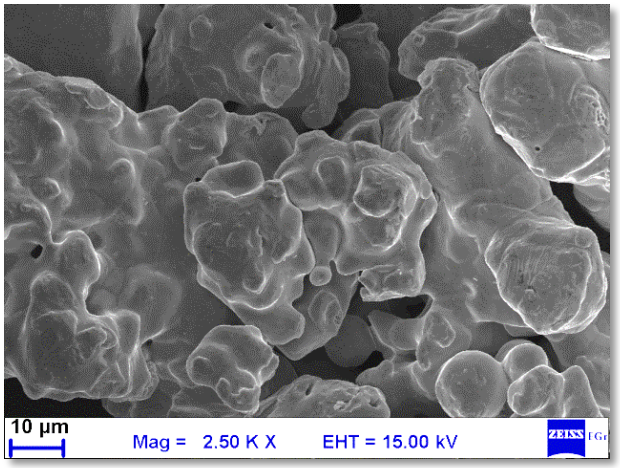

Figure 3 : SEM image of water atomized powder particle (irregular shape and rough surface) from[19] (Courtesy of Seshendra Karamchedu)

This irregular shape of the powder particles provides interlocking between them during compaction, which contributes to the green strength of the compact. Iron powders produced by this technique are of relatively low purity because of the surface reaction of powder particles with water steam in atomizer favours the formation of oxide layer on the surfaces. These powders are hence annealed in a continuous furnace to soften them and to reduce the surface oxide.

2.1.2 Alloying

Alloying addition improves the properties and performance of the PM steel components. In case of water atomized steel powders, alloying is done by admixing, prealloying or diffusion bonding or a combination of these, depending on the alloying elements and the final requirements. By utilizing a proper alloying technique, desired properties can be attained.

2.1.2.1 Admixing

The iron powders prior to compaction are admixed with alloying elements in the form of powders and usually graphite is added as a carbon source. The main advantage of this process is that the alloying composition can be altered with ease and the powder mixes have good compressibility. The drawback of this process could be segregation of the alloying elements which can result in heterogeneous microstructures upon sintering. Also by this process, along with the alloying elements, additives and lubricants are added before compaction.

2.1.2.2 Prealloying

This method involves the addition of alloying elements to the melt before atomization, and thereby achieving a homogenous distribution of alloying elements, see Figure 4(b). Prealloying typically reduces the compressibility of the powder. Molybdenum is the most common alloying element used for prealloying due to its relatively low effect on the compressibility. Also, Mo-prealloyed powders are used as a base powder for diffusion bonding of other alloying elements, such as Ni and Cu. Oxidation sensitive alloying elements, such as Cr and Mn, are introduced in prealloyed form to avoid the formation of surface oxides during water atomization since prealloying reduces their oxidation activity.

2.1.2.3 Diffusion Alloying

In this process, the alloying elements are mixed with the base powder (pure or prealloyed) and heated in a continuous furnace below the melting point in a reducing atmosphere, whereby the alloying elements (i.e. Ni, Cu, Mo) are diffusion-bonded onto the surface of the base powder, see Figure 4(c). Normally, elements that are not sensitive to oxidation are used for diffusion alloying. Diffusion alloyed powders exhibit good compressibility, compared to prealloyed powder. During sintering, homogeneous distribution of the alloying elements will take place. In the present work, Distaloy HP powder grade in which Ni and Cu are diffusion bonded to Mo-prealloyed powder (Astaloy Mo) is used as the base material for investigations.

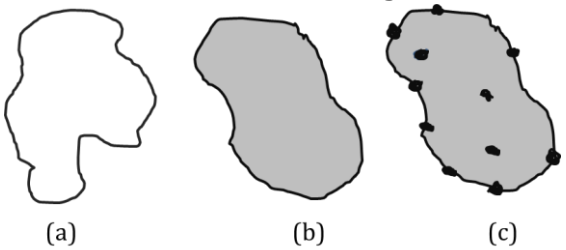

Figure 4 : Water atomized pure iron powder (a), prealloyed powder (i.e. Mo) (b), and diffusion bonded (i.e. Ni, Cu) prealloyed powder (c)

2.1.3 Compaction

Densification of the powder particles into component shapes is typically performed by uniaxial die pressing. The admixed powder is filled uniformly into the die cavity with the movement of top and bottom punches under a compression pressure of typical 500-800 MPa in order to achieve the final shape of the compacts. Upon compaction, the irregular powder particles interlock along with some degree of cold welding and so provide sufficient green strength to the component, which makes handling easier before sintering.

2.1.4 Sintering

In the conventional PM route, ferrous compacts are sintered at temperatures of around 1120°C to create bonding between the powder particles through solid state sintering. The parts are heated to around 450-600°C to remove the lubricants and other additives and then heated until sintering temperature. Sintering is performed in a controlled reducing atmosphere. High temperatures, up to 1250°C, are also used for sintering in some cases. In the initial stages of sintering, while heating up to the sintering temperature, reduction of surface oxides is achieved and the bonding between the powder particles takes place through the formation of inter-particle necks at the particle contacts through diffusion mechanisms.

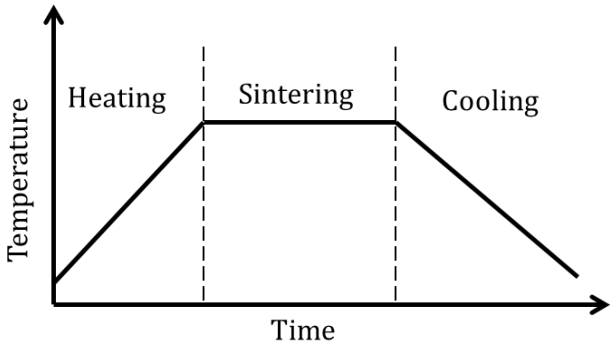

Figure 5 : A schematic sketch of sintering stages and time-temperature profile

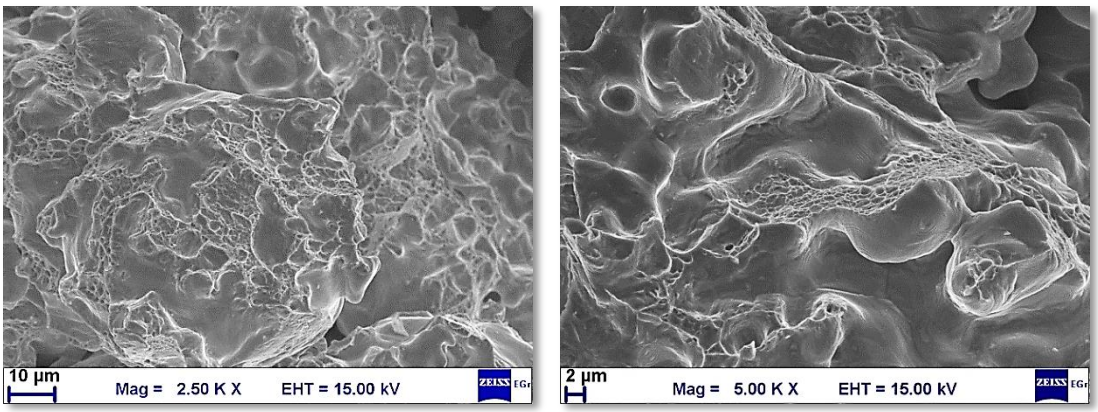

(a) (b)

Figure 6 : SEM micrographs showing the fracture surface of the PM compact after sintering, showing different cases of inter-particle fracture.

The strength of PM steel is determined by the strength of the inter-particle necks attained upon sintering which depicted in Figure 6. The main driving force behind inter-

particle neck growth is the surface energy reduction upon sintering. The compacts are loaded into the continuous furnace (belt-, walking beam- or pusher furnace, etc.) where they pass through the different heating zones and finally reach the cooling cycle in which the component microstructure is attained depending on the alloying elements and the cooling conditions.

2.1.4.1 Sinterhardening

Typically the microstructure of the PM steel after sintering consists of ferrite and pearlite after slow cooling in the furnace.in order to obtain martensitic microstructure, additional heat treatment (hardening) has to be performed. Whereas, in sinterhardening, hardening takes place right after sintering in the continuous furnace by rapid cooling the compacts and the typical cooling rate being 2-3 K/s in a neutral atmosphere in order to get martensitic microstructure. Hardened or sinterhardened parts require tempering to relieve the stresses which are incorporated within martensite. The main advantage by sinterhardening is to avoid an additional hardening process (heating and oil quenching). This reduces the cost of the components as well as potentially lowers the distortion. As sinterhardened parts are tempered in air rather than quenching, the quench oil retention is avoided and thus eventually improves the surface appearance [20]–[22]. In-line with the aforementioned advantages, in modern practice, base powder alloy design is performed in a way to comply with the sinterhardening characteristics of the modern furnaces.

2.1.5 Tempering

As it has been mentioned above, the hardened PM steels are tempered to relieve internal stresses. As a result of tempering, the toughness and ductility of the material are improved with a drop in hardness. Tempering of martensite will be discussed in detail in the following Chapter 2.3.3.4.

More than half of the produced PM steel tonnage go through some heat treatment to improve their final properties for a better performance [11].

2.1.6 Fractography of Sintered Steels

Fractured surface of the PM steels are characterised and can broadly be divided into four principal modes of fractures as below [23]

- Dimple rupture
- Cleavage rupture
- Decohesion rupture
- Fatigue

PM Steels possess microstructural discontinuities which influence initiation, growth and propagation of cracks. The fracture modes provide us a better understanding of the behaviour of the PM steels.

2.2 Creep in General

2.2.1 Introduction

The term creep is defined as time dependent plasticity under constant stress or loading conditions at elevated temperatures. It is an important design consideration for structural and high temperature applications. Normally, any material under applied load/stress will deform elastically and then plastically once it crosses the yield limit. Here the material deformation takes place at stresses below the yield limit under the influence of constant stress and temperature over a sustained time period. Creep in general occurs at homologous temperature $T/T_m>0.5$ for metals, where T is absolute temperature of application and T_m is absolute melting temperature.

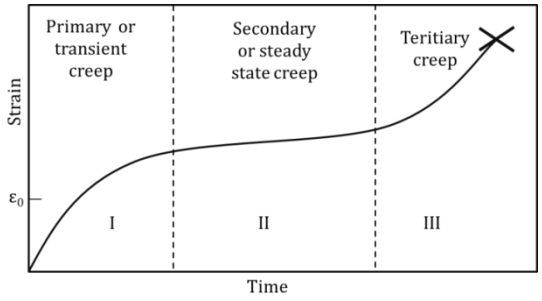

Figure 7 : Creep curve, Strain vs. time plot with different stages of creep [24]

With increasing temperature, the rate of deformation increases as a function of material properties, exposure time, temperature and applied stress. Eventually, over a period of time, the component loses its functionality, and it can eventually result in failure [24]–[26]. A typical creep curve, as shown in Figure 7, exhibits three stages of deformation, where in primary stage, the strain rate increases rapidly with instantaneous loading due to the work hardening and reaches minimum and the secondary or steady state creep where the strain rate is constant over a prolonged time period before it fails in the tertiary stage with accelerating strain rate. In the following chapters the influence of microstructure, stress and temperature are discussed since all these parameters play a vital role in creep behaviour.

2.2.2 Low Temperature Creep

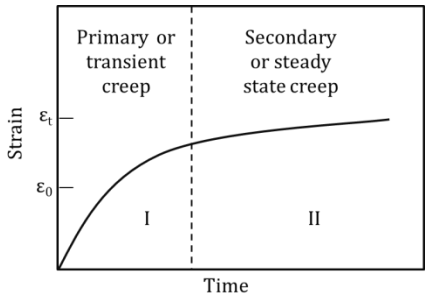

Figure 8 : Low temperature creep curve exhibiting only up to secondary stage [24]

Creep behaviour at homologous temperature $T/T_m<0.3$ is termed as low temperature creep. In case of low temperature creep, the component doesn't fail and constitutes only two stages of creep (primary and secondary stage) as seen in Figure 8. A few studies

have been carried out as these changes normally are neglected unless it constitutes a significant impact on the materials performance in applications. With increased demands for high performance applications, components precision is of high interest. Low temperature creep is observed in the case of pure metals around 0.1 – 0.2 T_m [9], [10]. However, there are some studies indicating a number of materials exhibiting such phenomena at these relatively low temperature and loads below the material yield strength, as reported in Table 1 and Table 2.

Table 1: Studies of low temperature creep behaviour on bearing steels[1]–[3]

Reference thesis	Year	Material	T in ℃	Stress in MPa	Time in hours
P. V. Morra PhD thesis	2003	Hardened and tempered Bearing steel	75-145	100-500	~70
Man-Nhi Tan Master thesis	2006			300-2000	
Jessica Nyqvist Master thesis	2007				

Table 2: Research articles on low temperature creep on steels and other materials [4]–[7], [9], [27]–[31]

Reference articles	Year	Material	T in ℃	Stress in MPa	Time in hours
L. B. Getsov	1971	Steels	20-500	600-800	~300
V. A. Likhachev *et al.*	1981	Hardened steel		175	
K. R. Williams *et al.*	1984	Mild steel	360-400	200-500	~4000
H. B. Chandler	1984	Mild Steels	room	150-210	
		Copper		55-75	
V. Sanchez-Galvez *et al.*	1985	cold drawn Steel wire	40-60	60-70% UTS (978-1141)	
T. H. Alden	1986	Stainless steel	25	250	~ 0.3
R. W. Neu *et al.*	1992	4320 steel	70-195	500	~150
A. Oehlert, *et al.*	1993	HSS	23	50% Y.S	~ 0.33
Cheng Liu *et al.*	2000	HSS	7± 2	~0,33 Rp0.2 (640)	80
U.H.Kivisäkk *et al.*	2008	Stainless steel	25	90% Rp0.2	24-100, ~600
Zhang Li *et al.*	2008	Titanium TA2	150	50-75% Y.S	100-1500

2.2.3 Creep Mechanisms

In case of pure metals at low temperatures, creep is controlled by the dislocation movement i.e. dislocation gliding and climbing, and at high temperatures diffusion plays a major role i.e. diffusional creep, termed as power-law creep. In the case of alloys, creep is entirely dependent on the complexity of microstructure which involves combined mechanisms of creep [2], [3], [24], [25]. The creep behaviour at low temperatures is only up to secondary stage of creep and it does not reach the tertiary stage i.e. the specimen will not fail, as seen in Figure 8. For low temperature creep, the strain varies as a logarithmic function of time. Upon loading, the creep reaches instantly the transient stage and continues to steady state only under the application of higher stresses according to the following equation

$$\boldsymbol{\varepsilon_t = \varepsilon_0 + \alpha \ln(t)} \text{ ------- (1)}$$

Where, $\boldsymbol{\varepsilon_t}$ is total strain, $\boldsymbol{\varepsilon_0}$ is initial strain up on loading and $\boldsymbol{t}$ is time in seconds and $\boldsymbol{\alpha}$ is creep parameter which depends on temperature.

2.3 Factors influencing Creep

The factors influencing the phenomenon of creep are:

- Temperature
- Stress (loading conditions)
- Microstructure
- Residual stresses

2.3.1 Temperature influence

Figure 9 shows the strain vs. time curves with increasing temperature at a constant stress which reveals that creep is a thermally activated process. The strain rate increase is evident at higher temperatures irrespective of the loading and microstructural conditions.

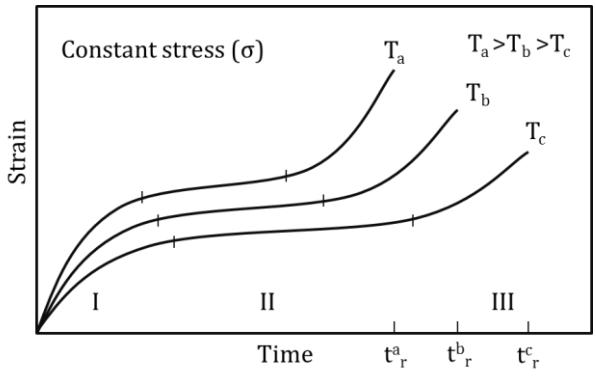

Figure 9 : Creep curves at constant stress with varying temperature, redrawn from [24]

2.3.2 Stress influence

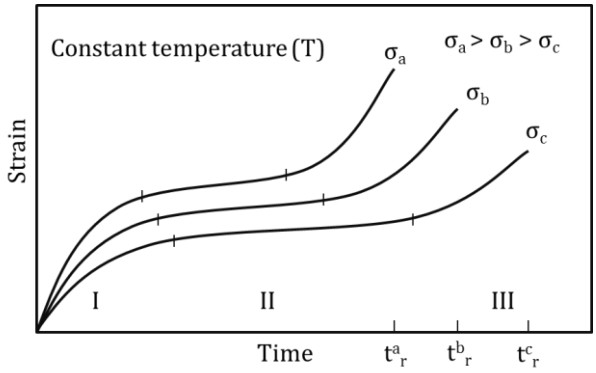

Figure 10 : Creep at constant temperature with varying stress, redrawn from [24]

Figure 10 shows the strain vs. time curves with varying stresses at a constant temperature showing that creep is stress dependent and with increasing stress the strain rate increases.

2.3.3 Microstructural influence

Irrespective of the loading and the temperature conditions, the microstructure plays a major role in the creep behaviour of the materials. Mechanism of creep depends upon the complexity of the microstructure since each microstructure has its unique characteristic creep behaviour. In the case of steels, hardened and tempered steel components are used for load bearing structural applications which are composed of martensite, bainite and retained austenite phases in the microstructure which will be discussed in detail in the following sub-sections.

2.3.3.1 Bainite

Bainite formation occurs above the martensitic start temperature and is classified into lower and upper bainitic structures. Bainite is a mixture of ferrite and carbide phases formed by diffusional mechanism upon cooling.

2.3.3.2 Retained Austenite

The martensitic transformation is not complete upon quenching, some austenite remains untransformed between the martensitic plates. This experiences high stresses due to the volume expansion of the martensitic phase that tends to trap and retain the untransformed austenite between the plates. The amount of austenite content left after the martensitic transformation is unstable at room temperature. This so called retained austenite will remains as an unresolved phase.

Retained austenite content in the components, when applied under high loading conditions or at elevated temperatures, will results in phase transformation associated with volume expansion causing dimensional instability. This can be eliminated by high temperature tempering whereby the residual austenite is transformed to ferrite and

cementite. Sometimes deep cooling/cryogenic treatment is carried out after hardening to transform the retained austenite into the martensite.

While austenite is unstable at room temperature, as mentioned above, it has a potential to influence the stability of the structural components in applications upon its existence exceeding certain maximum level. So, the retained austenite content is normally maintained below certain nominal value. [32], [33].

2.3.3.3 Martensite

Martensite formation is a result of diffusionless transformation and it is a metastable phase. Formation of martensite involves heating the steel to austenizing temperature with a subsequent rapid quenching in liquid or gas. During the rapid cooling, the diffusion is inhibited.

The steel is heated to form austenite, which is a supersaturated phase (FCC) with a high solubility of carbon. When austenite is slowly cooled, it will transform to BCC-ferrite wherein the carbon dissolution is limited, and the rest of the carbon precipitates into cementite. In order to avoid such a diffusional transformation, the steel is quenched rapidly from austenitic temperature to a temperature below martensitic start temperature, which depends on the alloy composition and especially carbon content. The resulting martensitic phase is BCT (body centered tetragonal) structure enriched in carbon. This transformation causes lattice displacement and distortion and, as a result, there will be an overall volume expansion with contraction in the z-axis up to 20% and expansion in both x and y – axes up to 12% in the BCT crystal structure. This transformation is a result of pure shear mechanism. Two types of martensite morphology can be formed: lath and plate martensite, depending on the carbon content and cooling rate.

$$\text{Austenite}(\gamma)\ fcc \rightarrow \text{martensite}\ (\alpha')\ bct$$

The hardness of martensite is a result of solid solution strengthening by the interstitial carbon atoms as well as the lattice deformation and twinning which result in high dislocation density that can act as a potential barrier for the dislocation movement. The hardness of martensite is around 50-60 HRC, and it is also very brittle with a high amount of stored free energy [26], [32]–[34].

2.3.3.4 Tempering of Martensite

Tempering is the post-hardening heat treatment process carried out to improve the strength and toughness of the hardened material, as a result of which a decrease in the hardness and an increase in the ductility of the material is attained. Tempering involves heating the material to a temperature much below the austenization temperature for a period of time (in the order of an hour) either in a particular controlled atmosphere or in air. Hardened steels shrink upon tempering because of the martensite decomposition into ferrite and carbide phases. Also, retained austenite will transform into ferrite and

cementite when tempered between 200-350°C [22], [33], [35], [36]. Table 3 lists the transformation processes occurring at different tempering temperatures.

Table 3: Transformation during tempering temperatures from [33]

T°C	Transformation
20-100	Carbon segregation to dislocations and boundaries, Clustering of carbon atoms on octahedral sites of martensite
100-200	Precipitation of transition carbide as aligned particles
200-350	Transformation of retained austenite to ferrite and cementite
250-350	Lath like Fe_3C precipitation
350-550	Segregation and cosegregation of impurities and substitutional alloying elements
400-600	Recovery of dislocation structure – elimination of dislocation tangles and cell walls
500 -700	Formation of alloy carbides in alloyed steels

3 Materials and Experimental Procedure

The material used for the investigation, the experimental techniques applied and the analytical methods utilized are described in the following sections of this chapter.

3.1 Material

Distaloy HP is a water atomized diffusion alloyed powder grade from Höganäs AB, Sweden. It is a commercially available high performance powder grade with 4 wt.% Ni and 2 wt.% Cu diffusion bonded to steel powder pre-alloyed with 1.5 wt.% Mo.

Table 4 : Nominal Composition in wt.% of the investigated powder

Powder Grade	Ni	Cu	Mo	Fe
Distaloy HP	4	2	1.5	Balance

The base powder is mixed with 0.6wt.% graphite as a carbon source and 0.6wt.% Kenolube as a lubricant and then compacted into standard tensile specimens according to MPIF10 [37] and were produced by Höganäs AB, Sweden. The specimens are sintered at 1120°C in 90% N_2/10% H_2 atmosphere and sinterhardened at a cooling rate between 2.5 and 3°C/s. Some specimens are subsequently tempered at 200 and 300°C in air for 1 hour.

Table 5 : Designation of different sintered samples based on Distaloy HP (DHP), sinterhardened and further deep cooled and/or processed at different tempering conditions

Sample denomination	Descriptions
DHP-UT	Sinterhardened without tempering (Untempered)
DHP-T200	Tempered at 200°C for 1 hour in air
DHP-T300	Tempered at 300°C for 1 hour in air
DHP-DC-UT	Deep cooled in Liquid N_2 without tempering (Untempered)
DHP-DC-T200	Deep cooled in Liquid N_2 and Tempered at 200°C for 1 hour in air
DHP-DC-T300	Deep cooled in Liquid N_2 and Tempered at 300°C for 1 hour in air

Table 5 describes the processing conditions employed for the different samples investigated in this study. The sample denominations used in Table 5 will be used for different samples in the rest of the thesis. The tensile tests were carried out to obtain the mechanical properties and also to obtain the fracture surface on which fractography studies has been performed.

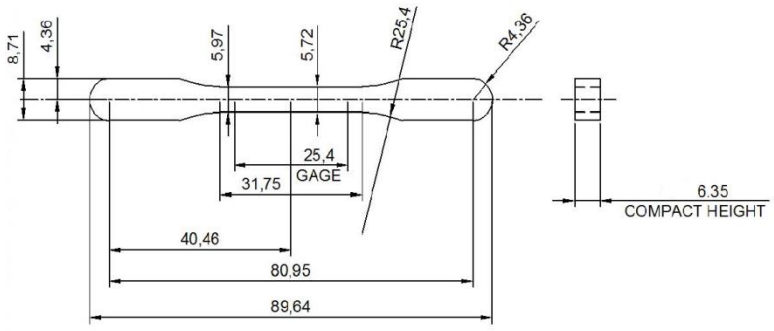

Figure 11 : Tensile specimen dimension according to MPIF10 redrawn from [37]

3.1.1 Experimental Methods

The experimental techniques utilized are listed in the Table 6 and a detailed description of these techniques is discussed in detail in the following sections.

Table 6 : List of experimental and analytical techniques utilized

Experimental and analytical technique	Performed investigations
Universal Materials testing machine with temperature controlled environmental chamber	Tensile testing Creep testing Cyclic creep testing (varying temperatures)
Light optical microscopy	Microstructural investigation and imaging
Scanning electron microscopy combined with EDX(Energy Dispersive X-ray spectroscopy)	Fractography Elemental mapping Chemical analysis (qualitative analysis) Microstructural analysis
Hardness testing	Apparent hardness and microhardness
X-ray diffraction	Retained austenite content measurement

3.2 Universal Material Testing

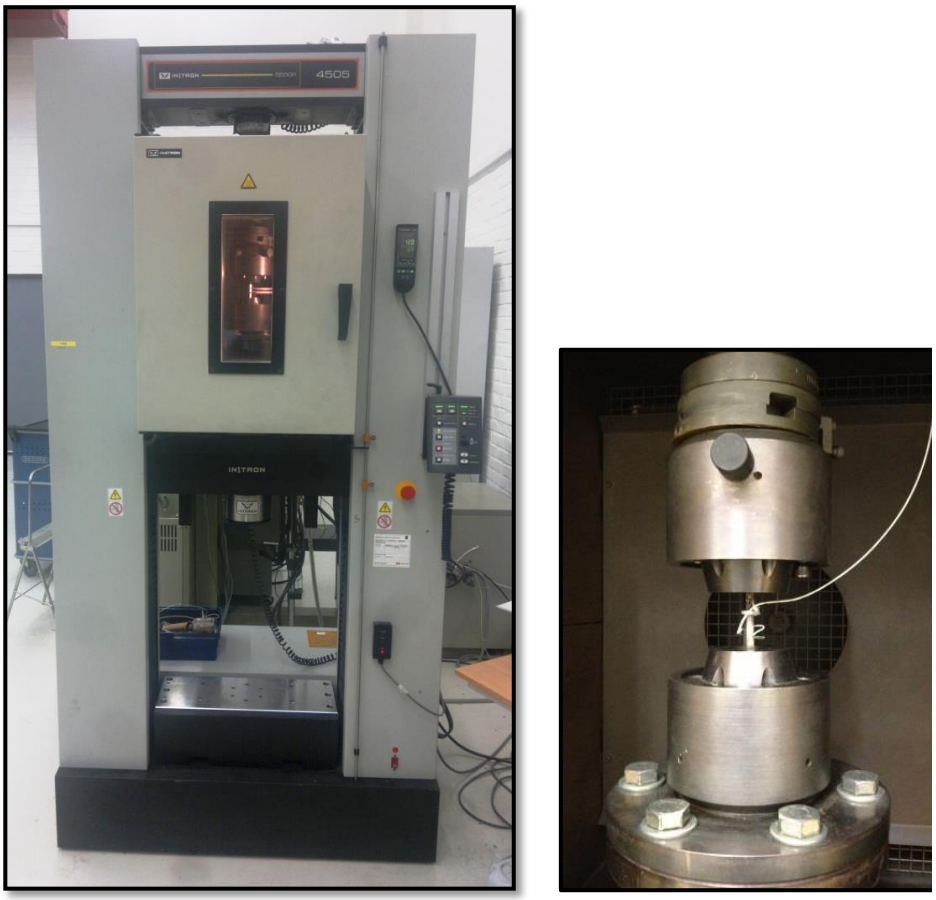

(a) (b)

Figure 12 : (a) Tensile testing machine with environmental chamber and (b) Sample connected to thermocouple clamped in between jaws

An electro-mechanical testing machine *Instron 5500R with 4505 load frame* was used for tensile and creep/relaxation tests. It is equipped with Instron 3119-407 environmental chamber with a temperature controller unit, see Figure 12(a). The chamber has a temperature range between -150°C to 350°C. Blue hill software was used for data acquisition. During testing, the samples were carefully aligned vertically along the axis and the extensometer was carefully mounted. Once the sample is clamped between the jaws, the furnace door is closed and the temperature is set to the determined level. The approximate time to reach the steady state temperature (in our case 120°C) was determined by connecting thermocouple to the test specimen as shown in Figure 12(b). The time to reach steady state temperature was found to be approx. 90 min, with a variation of ±0.5°C in the beginning, after which a steady state temperature is maintained, (see Appendix 1). The tensile tests for fractography and some tests at 120°C were carried out at Chalmers with this machine at strain rate of 10-4/s. All creep tests were carried out at a constant load condition and temperature, also creep tests with varied temperature under fixed load were performed on this setup.

3.3 Scanning Electron Microscopy

High Resolution Scanning Electron Microscopy (HRSEM) imaging was performed using a *LEO 1550 Gemini* SEM equipped with In-lens and secondary electron detector for imaging. Qualitative chemical analysis was performed for different phases and elemental mapping and elemental line scans were performed to assess the elemental distribution by using X-MAX EDX detector attached to the SEM. SEM is the most commonly used technique for high resolution imaging due its high magnification and depth of focus capabilities, which is limited in the case of light optical microscopy. The fractured surfaces were analysed with a fixed voltage of 15 keV and working distance of 8 mm. All studies were carried out with these settings to characterise the materials based on the different heat treatment and the tempered conditions as presented in Table 5.

3.4 Metallography

The metallographic samples were prepared from the cross section of the tensile specimens before and after creep testing. All the cut pieces were mounted using *Polyfast* resin in a *Struers CitoPress-20* mounting machine. All the mounted specimens were ground, polished and etched according to *Struers* standard for metallographic preparation of PM parts. The etchant used was picral-nital (solution of 4 g of picric acid and 2 ml of Nitric acid in 200 ml of ethanol) to obtain a contrast between bainite and martensite. The microstructure of the samples was studied by light optical microscopy using *Leitz DMRX* light optical microscope equipped with *AxioVision* imaging software.

3.5 XRD – Retained Austenite Estimation

X-ray Diffraction (XRD) is a non-destructive testing technique used for determination of residual stresses (compressive or tensile), and for the identification of different phases and their amounts in the case of crystalline materials. The measurement principle is

based on the constructive and destructive interference occurring in the sample upon incidence of X-rays and according to the Braggs law, the interatomic distance is calculated:

$$2d \sin\theta = n\lambda$$

where n is order, d is interatomic distance, λ is wavelength of characteristic X-rays, and θ is the incident angle of X-rays Diffraction pattern is obtained from the outgoing X-rays, and each crystal has its own unique characteristic pattern based on the atomic arrangement. By referring to the available database the respective details are identified (phases, atomic structure, etc.).

In this study, the sample is irradiated with the incident X-rays to depths of about 6-7 µm. *XSTRESS 3000* was used to determine the austenite content using "ASTM E 975-03 Standard Practice for X-ray Determination of Retained Austenite in Steel with Near Random Crystallographic Orientation." The principle is based on the assumption that the total integrated intensity of all the diffraction peaks of a phase (here either ferrite or austenite) is proportional to its volume fraction. The amount of austenite is determined by considering four different crystalline peaks corresponding to two ferrite and two austenite phases. All the ferrite regions include martensite which is considered as BCC, whereas FCC phases are considered as austenite which includes both retained austenite and Ni–rich austenite. The austenite content analysis was performed on the tensile samples before and after creep testing to evaluate the percentage change in the austenite content. Moreover a few samples after deep cooling in liquid nitrogen were analysed.

3.6 Apparent Hardness

Hardness is the resistance to deformation or indentation. In case of PM steels, the hardness measurement includes both pores and the base material which gives the effect of porosity on a macro scale. Apparent hardness was measured using a *Wolpert Dia Testor* with a Vickers indenter using 10 kg load (HV10) according to the MPIF43 standard. The apparent hardness was measured for all the samples before and after creep testing for 1 million seconds.

3.7 Microhardness

Microhardness is measured on the individual phases which represent the hardness of the material/phase in the absence of pores. In the present investigation, microhardness of Ni-rich austenite, martensite and bainite regions were obtained individually for the samples at different conditions as shown in Table 5. All the measurements were performed using *Struers DuraScan 70* with automatic measurement software. Lower loads were used (50 g) for the case of Ni-rich austenite (HV0.05) due to its small area and higher loads of 100 g was used for the case of martensite and bainite (HV 0.1) which is according to the standard MPIF51.

4 Results

4.1 Tensile testing

Table 7 below shows tensile test results carried at Höganäs AB on the sinterhardened-tempered and sinterhardened-deepcooled-tempered samples. The yield strength according to 0.2% proof stress (Rp0.2), the ultimate tensile strength (Rm) and the percentage of elongation to failure were measured on 10 samples and the values are shown below in Table 7. DHP-T200 (sinterhardened and tempered at 200°C) exhibits highest ultimate tensile strength and percentage elongation which is around 1% that is substantial elongation for sinterhardened PM steels. In case of sinterhardened and tempered samples, the yield strength (Rp0.2) increases with increasing tempering temperature.

Table 7 : Distaloy HP Tensile testing results from Höganäs AB

Samples	Rp0.2, [MPa]	St.dv	Rm, [MPa]	St.dv	Elongation %	St.dv
DHP-UT	691	50	926.6	23	0.46	0.05
DHP-T200	807	48	1163	43	0.92	0.19
DHP-T300	853	36	1025	31	0.53	0.09
DHP-DC-UT	*	*	812	29	0.10	0.05
DHP-DC-T200	1008	28	1095	21	0.34	0.06
DHP-DC-T300	871	18	926	46	0.30	0.06

* it is too brittle

(a)

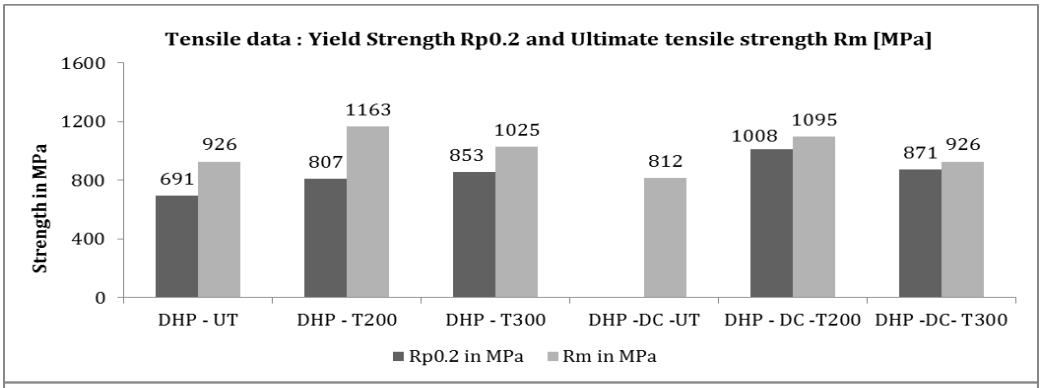

(b)

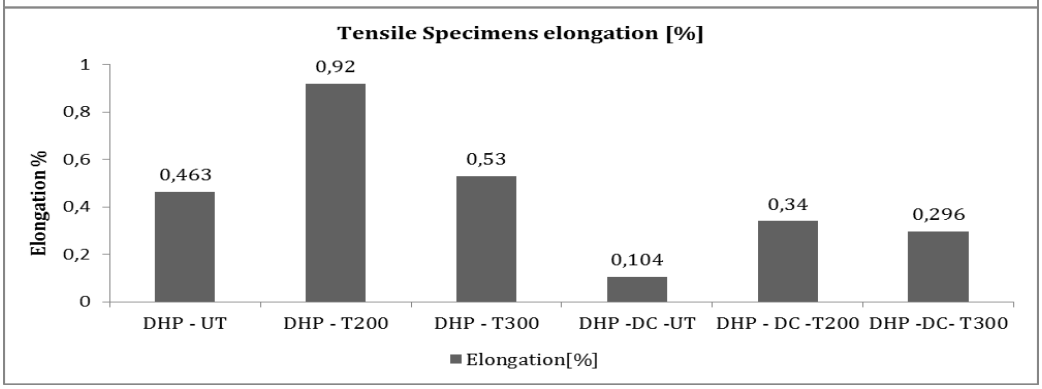

Figure 13 : Tensile test results of the samples showing yield strength and tensile strength (a) and elongation (b)

DHP-T300 exhibits high yield strength values among the sinterhardened-tempered samples with good ultimate strength and moderate ductility which actually corresponds to the microstructure upon higher tempering temperature.

In case of deepcooled samples DHP-DC-UT (sinterhardened-deepcooled-untempered), the samples are too brittle and fail before yielding. The DHP-DC-T200 sample exhibits very high yield strength among all the samples and good tensile strength. However, all the deepcooled samples exhibit poor ductility as compared to the sinterhardened-tempered samples.

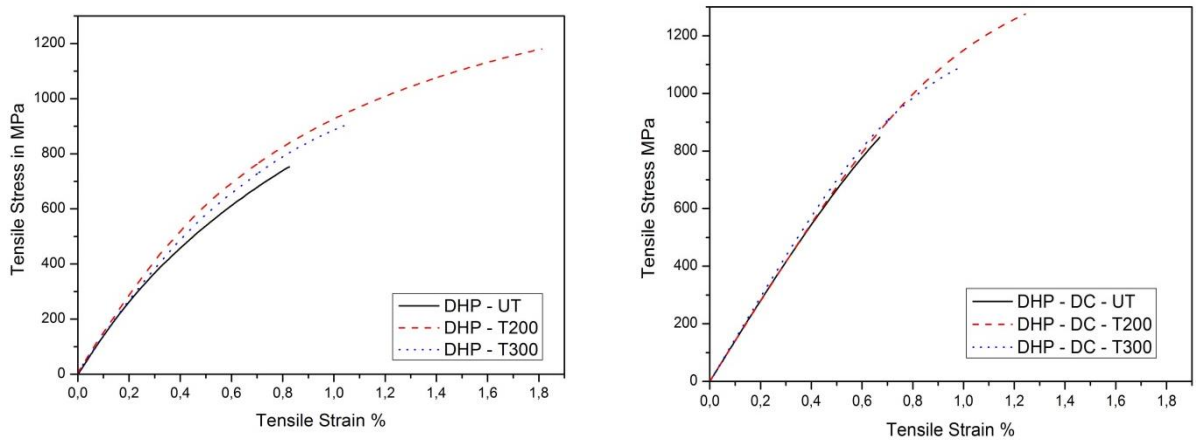

(a) (b)

Figure 14 : Tensile test results of sinterhardened and subsequently tempered samples (a) and sinterhardened-deepcooled-tempered samples(b) performed at Chalmers

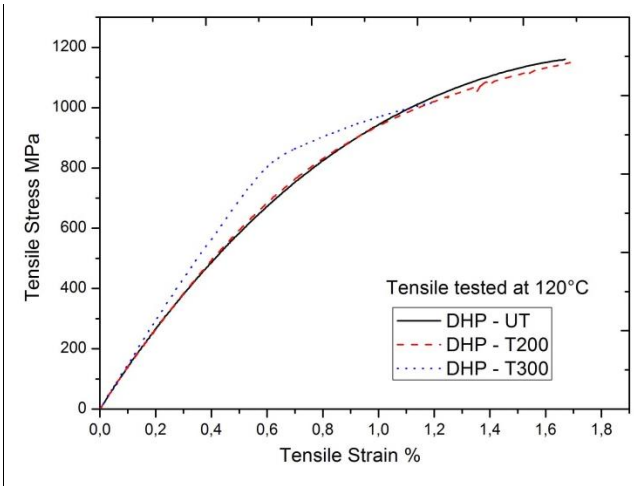

Figure 15 : Tensile testing of sinterhardened-tempered samples at 120°C

The tensile test carried out for each set of samples are summarised in Figure 14 and Table 8. These tests were performed for each condition to correlate the actual results from Höganäs AB and also to obtain the fracture surfaces for further fractographic investigation.

Table 8 : Tensile test results performed at Chalmers

Samples tested at room temperature	Rp0.2, [MPa]	Rm, [MPa]
DHP-UT	702	752
DHP-T200	827	1180
DHP-T300	850	909
DHP-DC-UT	*	848
DHP-DC-T200	1200	1276
DHP-DC-T300	1061	1094

* it is too brittle

Tensile tests on sinterhardened-tempered samples were also performed at 120°C, see Figure 15 and Table 9. At 120°C, DHP-UT and DHP-T200 samples exhibit increased yield strength, ultimate tensile strength as well as higher elongation. Whereas, DHP-T300 sample tested at 120°C exhibits similar properties as it tested at room temperature with only a slight increase in ductility.

Table 9 : Tensile results of sinterhardened–tempered samples tested at 120°C

Samples tested at 120°C	Rp0.2, [MPa]	Rm, [MPa]
DHP-UT	896	1161
DHP-T200	898	1150
DHP-T300	860	1036

The increased tensile properties of DHP-UT when tested at 120°C reveal the initial tempering effect at that temperature. It is important to evaluate the properties of the samples at 120°C as the creep experiments were performed at 120°C.

These tests gave a better understanding of the samples tested at room temperature and 120°C even though there is a slight variation in results. Samples tested at 120°C have improved tensile properties compared to the room temperature samples. Especially the DHP-UT samples are more sensitive to this temperature than the DHP-T200 and DHP-T300 ones. However, the tensile results carried out at room temperature from Höganäs AB form the basis for load selection of the following creep experiments in this study.

4.2 Fractography

The fractographic investigation was done on the fractured samples from the tensile testing of Distaloy HP material after different tempered conditions to understand the fracture behaviour and correlate the mechanical properties. The macroscopic investigation of the fracture surface of DHP-UT, obtained by stereomicroscope, is shown in Figure 16. It reveals a flat fracture surface with brittle failure, typical for PM steels, especially with martensitic structure. Macroscopic investigation in case of PM steels gives very limited information about fracture surface features.

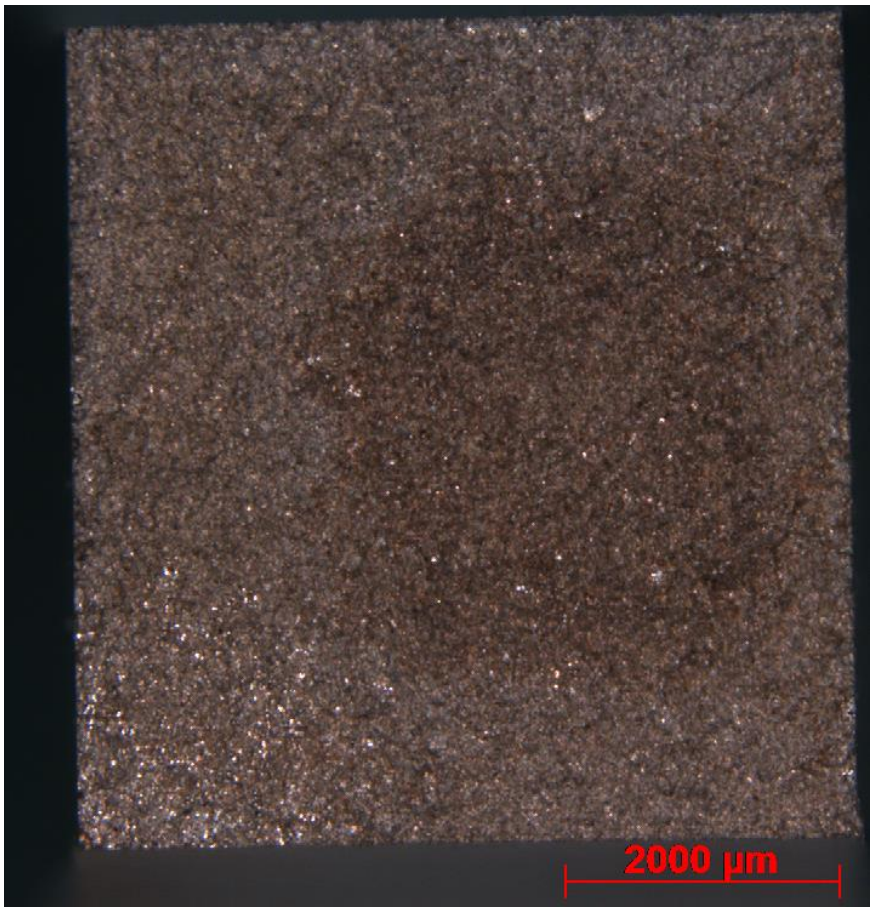

Figure 16 : Macroscopic view of fracture surface of DHP – UT specimen by stereomicroscope

Detailed microscopic investigation using HRSEM has been carried out to reveal the failure mechanism which is dependent on local microstructure characteristics, determined by tempering conditions. In the following chapter, the fractographic investigations of the samples are shown for the sinterhardened-tempered and sinterhardened-deepcooled-tempered samples.

4.2.1 DHP-UT

The fracture surface of the sinterhardened sample, i.e. DHP-UT sample, is shown in Figure 17, where (a) and (b) show the general appearance of the fracture surface. Fracture surface is rough and cluster of the prior powder particles can be distinguished.

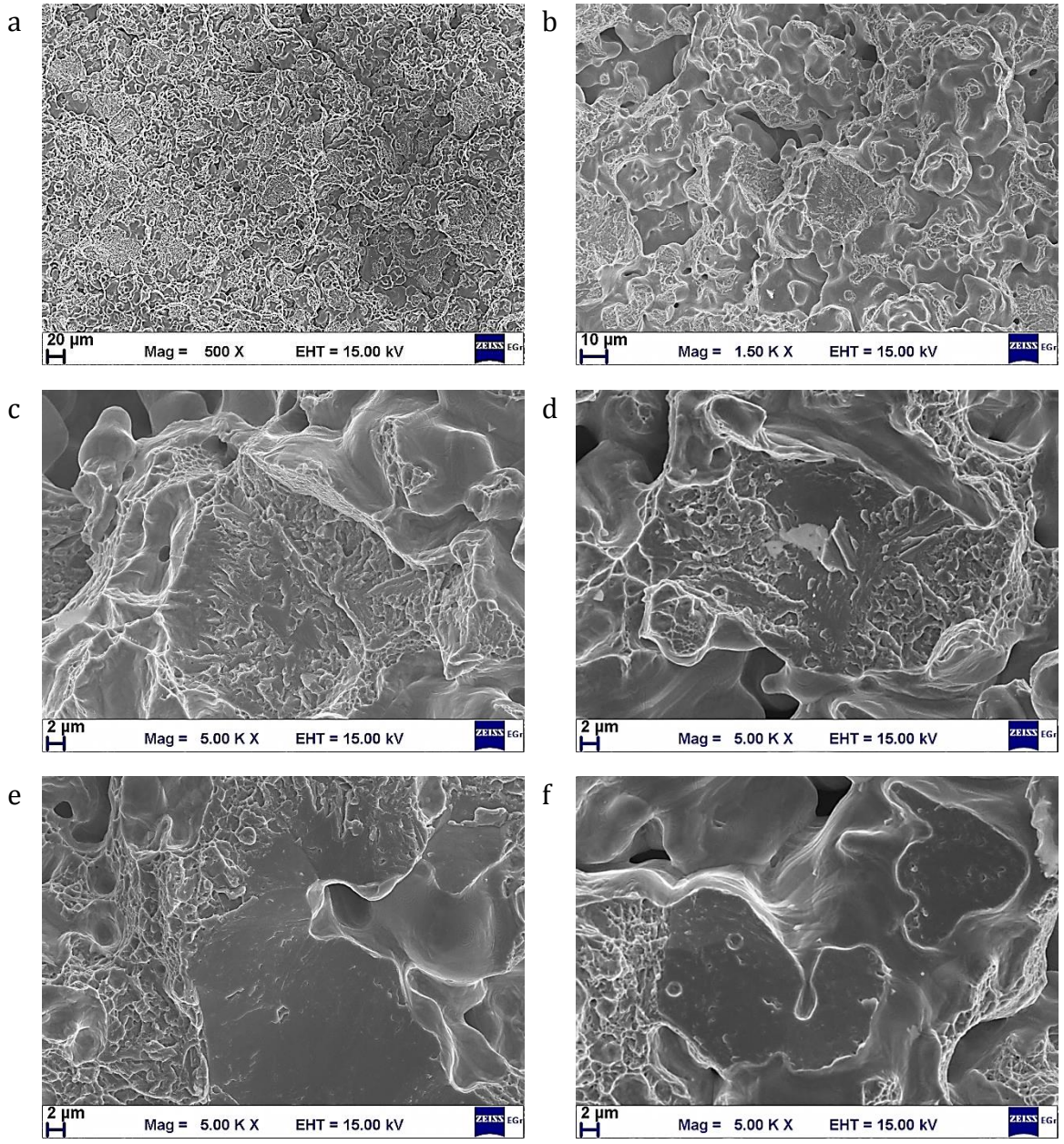

Figure 17 : Fracture surface of DHP–UT sample showing (a) the general rough appearance at lower magnification, (b) agglomerates of the powder particles (c) & (d) transgranular cleavage and semi cleavage facets, (e) transparticle decohesion failure, (f) interparticle decohesion failure.

Observation of the fracture surface at higher magnification reveals that the transgranular cleavage is the dominant failure mode in the sinterhardened-untempered specimen, see Figure 17 (c, d). Interparticle and transparticle ductile dimple fracture, see appendix, and more rarely interparticle decohesion facets, see Figure 17 (e, f), were also observed on the fracture surface of this specimen.

4.2.2 DHP-T200

From the fracture surface of the DHP-T200 samples, a rough appearance of the fracture surface is evident, see Figure 18 (a, b).

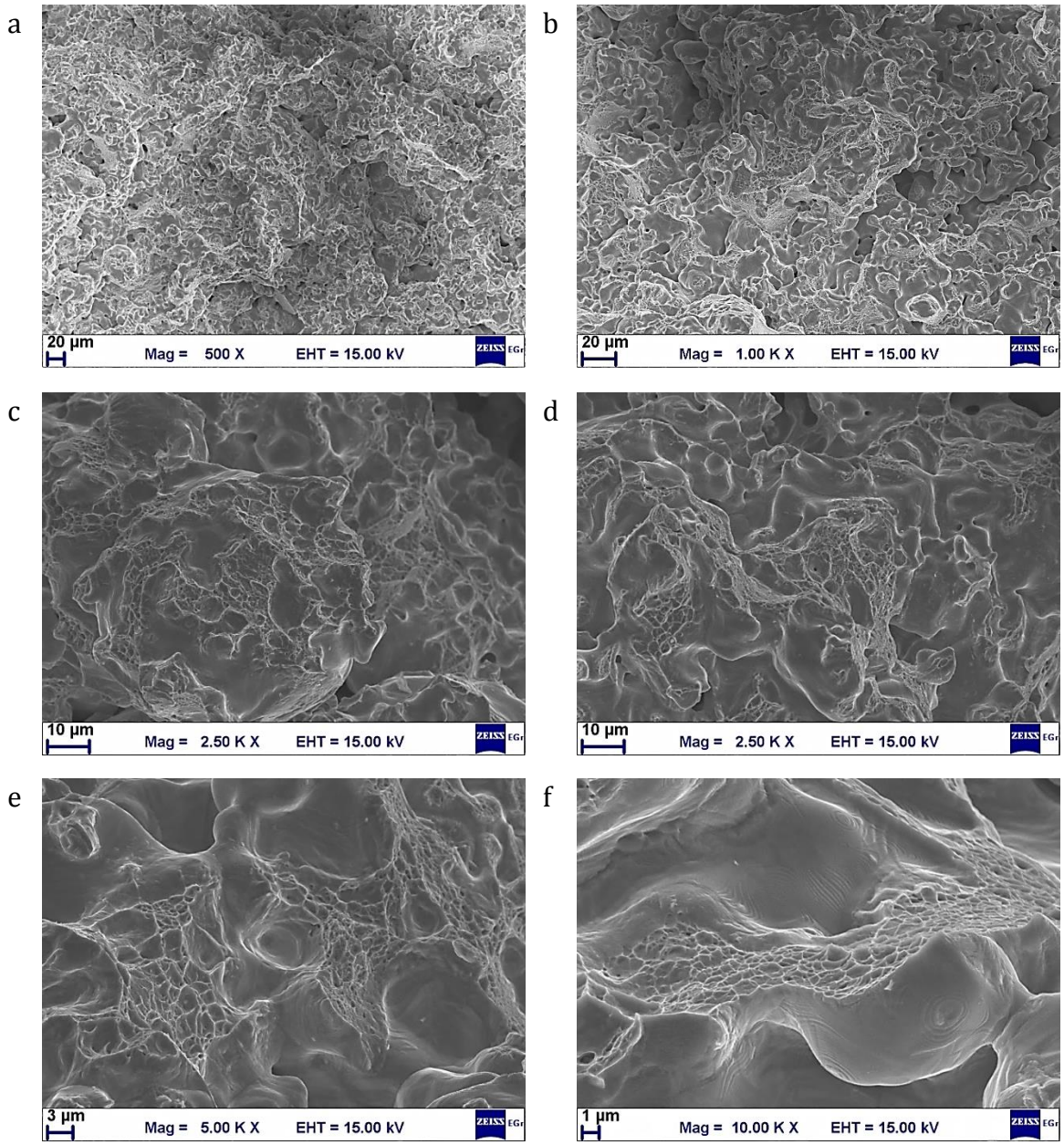

Figure 18 : Fracture surface of DHP–T200 sample showing the general appearance of fracture surface at low magnifications (a, b) and interparticle and transparticle ductile dimple fracture (c-f).

Dimple ductile fracture is the main failure mechanism for this specimen. Figure 18(c-f) shows appearance of different sites of interparticle and transparticle ductile dimple failure. Typically, in case of the interparticle ductile fracture, dimples are deeper as they are initiated by coarse oxide residues or bridge porosity inside interparticle necks, see Figure 18 (c, e). In the case of the transparticle ductile fracture dimples are shallow as they are initiated by fine carbides or fine internal oxides, see Figure 18 (d, f). In general the initial powder (pore) surface looks clean without any oxide particulates (see appendix for more detailed images).

4.2.3 DHP-T300

Similarly to previous specimens, roughness of the fracture surface was found for the DHP-T300 samples as well, see Figure 19 (a, b), where individual particles or agglomerates can be distinguished in some sites.

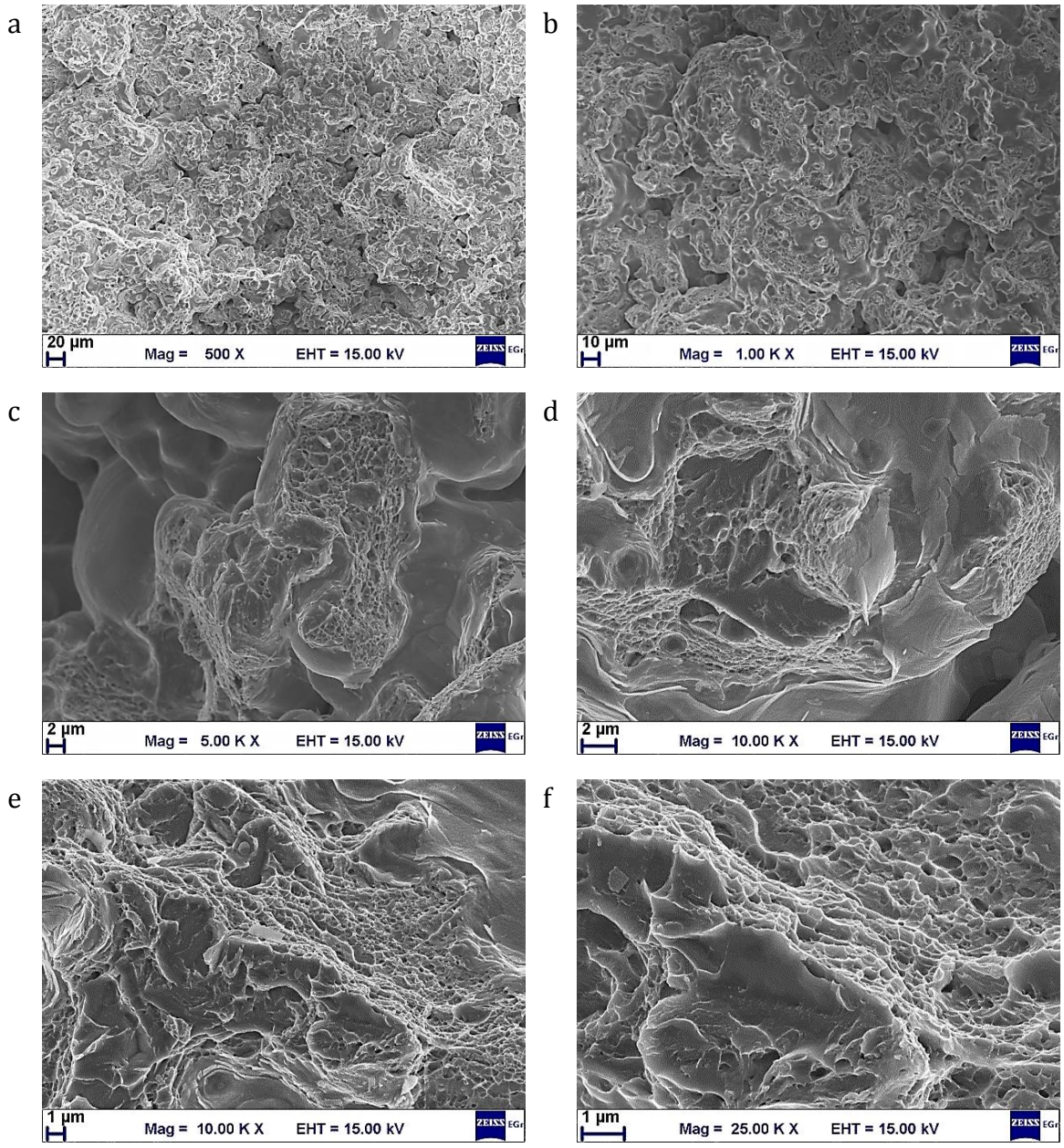

Figure 19 : Fracture surface of DHP–T300 sample showing the general appearance of the fracture surface (a, b) and (c-f) shows different sites of inter- and transparticle dimple ductile fracture together with cleavage fracture.

The failure mechanism is a mix of inter- and transparticle dimple ductile fracture with cleavage failure, see Figure 19 (e, f). The pore surface shows presence of thin iron oxide layer (flaky particulates and layers) due to oxidation during tempering in air. See Appendix 2 for more detailed images.

4.2.4 DHP-DC-UT

Fracture surface of the DHP-DC-UT sample has similar roughness as specimens without deepcooling, see Figure 20 (a, b).

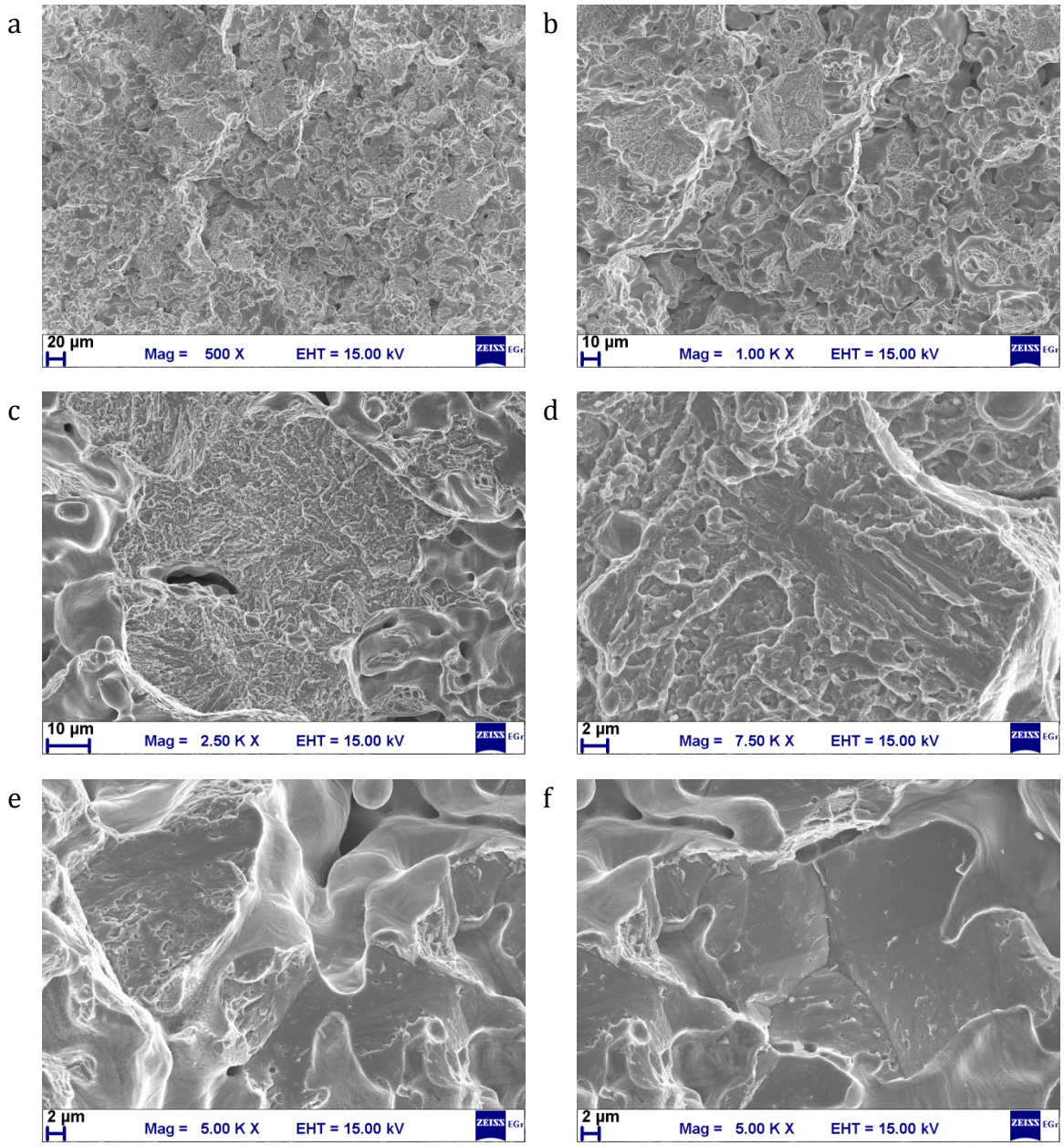

Figure 20 : Fracture surface of DHP–DC-UT specimen showing the general appearance of the fracture surface (a, b) and observed fracture mechanisms: transparticle transgranular quasi-cleavage (c, d) and inter and transparticle intergranular decohesion facets (e, f)

Cleavage and quasi-cleavage are the main fracture modes in case of this specimen. Inter- and transparticle intergranular decohesion facets were observed as well, see Figure 20 and Appendix 2.

4.2.5 DHP-DC-T200

Fracture surface roughness doesn't change after tempering of DHP-DC-, see Figure 21 (a, b).

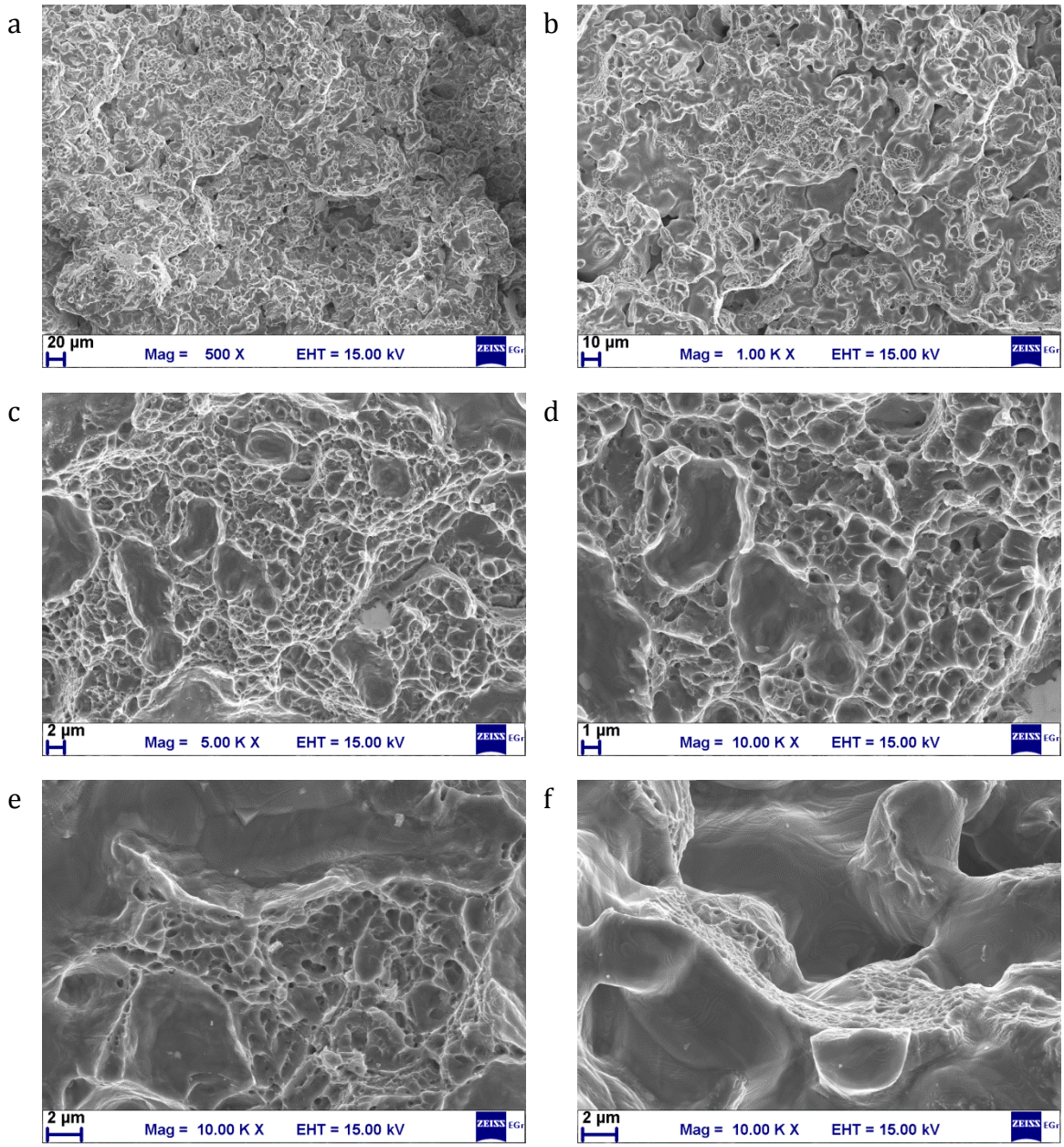

Figure 21 : Fracture surface of DHP–DC-T200 specimen showing roughness of the fracture surface (a, b) and main fracture micro-mechanisms, namely interparticle(c-e) and transparticle dimple ductile fracture (f).

Dimple ductile fracture seemed to be the dominant failure mechanism observed in this sample, see Figure 21 (c-f) and Appendix 2.

4.2.6 DHP-DC-T300

Fracture surface of DHP-DC-T300 sample looks rather rough where large powder agglomerates can be distinguished, see Figure 22 (a, b).

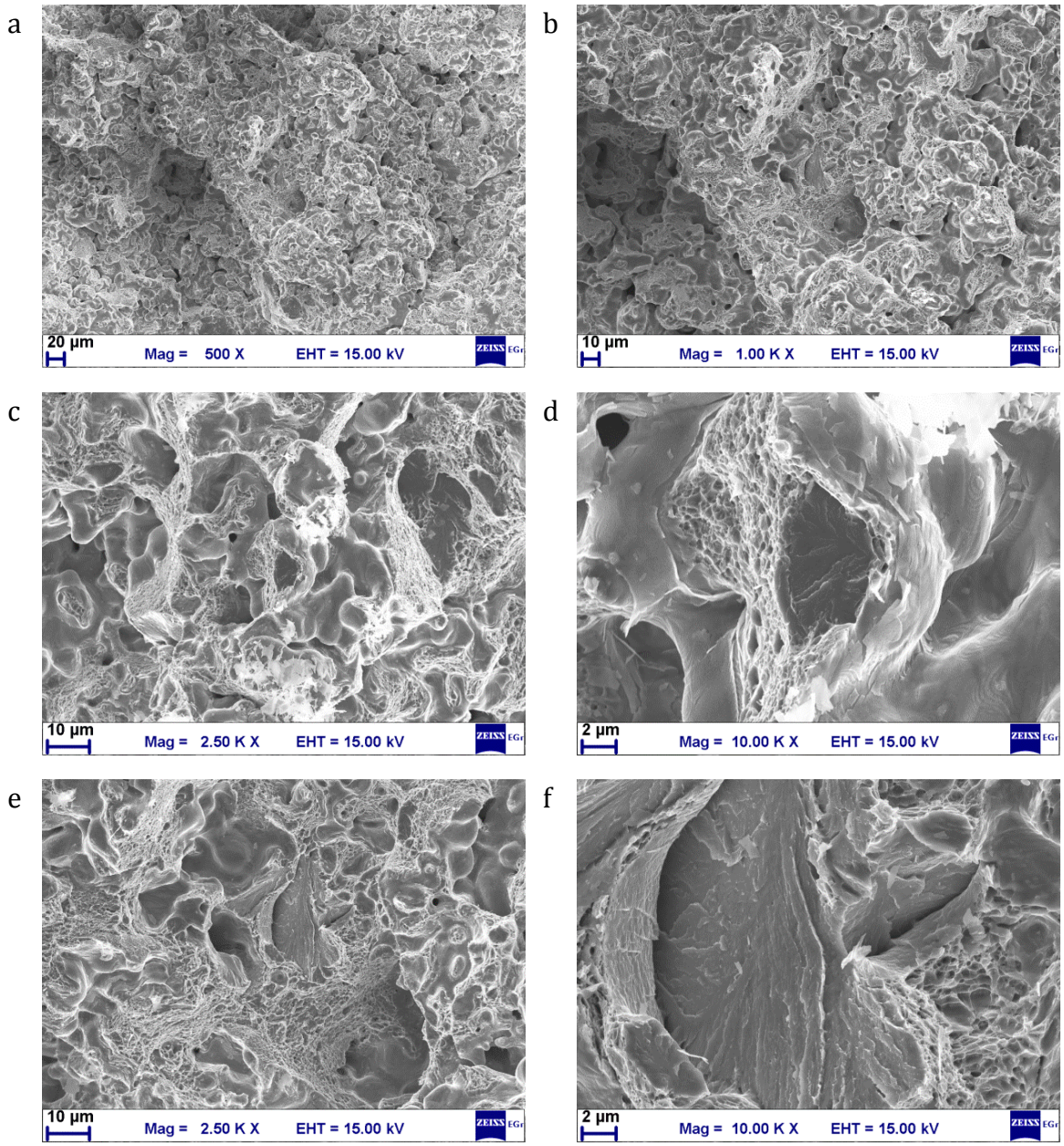

Figure 22 : Fracture surface of DHP–DC-T300 specimen showing the general appearance of the fracture surface (a, b) and transparticle transgranular cleavage (c, d) and inter and transparticle dimple ductile fracture (e) and transgranular cleavage with river patterns (f).

The failure is mainly due to the transgranular cleavage and transgranular dimple ductile failure, see Figure 22 (c-f). Free powder surface (pore surface) is oxidised as well, which is typical for specimens tempered at 300°C in air. More SEM micrographs of the fracture surface for this specimen can be found in the Appendix 2.

4.3 Metallography

Microstructures of sinterhardened-tempered and sinterhardened-deepcooled-tempered samples are presented below. The typical microstructure of the Distaloy HP is heterogeneous structure consisting of martensite (M), bainite (B) and Ni-rich regions (N) observed as a white constituent with characteristic pores, for an example see Figure 23. The heterogeneous microstructure is distributed homogenously throughout the cross section of the sample.

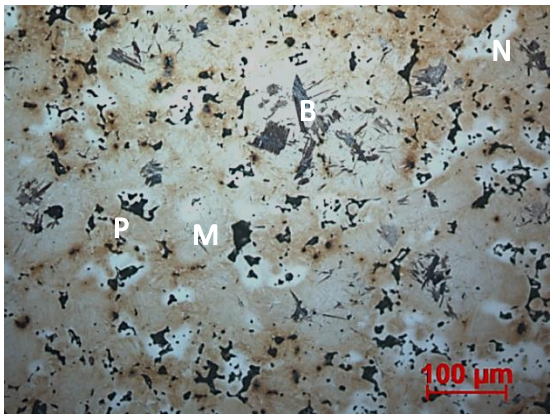

M-Martensite

B-Bainite

N-Ni rich region

P-Pore

Figure 23 : Typical microstructure of Distaloy HP material

From Figure 24 and Figure 25, the martensitic plates with bainitic regions and the islands of white regions (Ni-rich) can be observed in DHP-UT and DHP-T200 samples. The optical microscopy images of the etched DHP-T300 samples show tempered martensitic(TM) regions, which consists of higher fraction of bainite as shown in Figure 26. The Ni-rich regions (white areas) are surrounded by the martensitic regions as shown in the figure. Tempered martensite is difficult to differentiate from previously observed bainitic areas in this case. The existence of Ni-rich regions at this tempering temperature emphasizes the stability of this phase.

In case of deepcooled DHP-DC-UT and DHP-DC-T200 samples, the microstructure is rather similar to the respective tempered samples without deepcooling as shown in Figure 27 and Figure 28. DHP-DC-T300 also shows similar heterogeneous microstructure as previous samples (i.e. DHP-T300). However, tempered martensite is more visible as the darker contrast between martensitic plates/laths which is due to precipitation of transition carbides. The tempered martensitic phase and the precipitates of carbides can be clearly observed in the Figure 29. In this sample, it is considered that there is no retained austenite phase, since the sample is deep cooled in liquid N_2, which completes the martensitic transformation. Moreover, the tempering at 300°C is expected to facilitate full transformation of residual austenite (if any) into ferrite/carbide mixture.

Hence the microstructure of all the six samples exhibits their characteristic microstructure with respect to the synthesis condition and the tempering temperatures. However, it is difficult to distinguish the retained austenitic phase from the microstructure and it is considered that retained austenite is entrapped between the

martensitic plates with different appearance and size fraction compared to the Ni-rich austenite. Retained austenite between the martensitic plate's transforms into ferrite and transition carbides that together with precipitation of transition carbides from martensite upon tempering at high temperatures. It will transform to martensite upon deepcooling in liquid N_2 depending on the treatment of the specimen.

DHP-UT

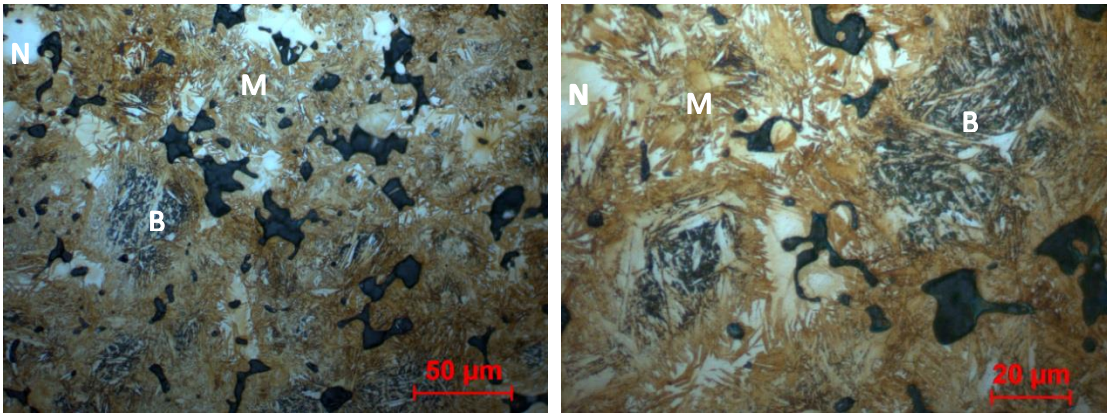

Figure 24 : Microstructure of DHP-UT sample at different magnifications

DHP-T200

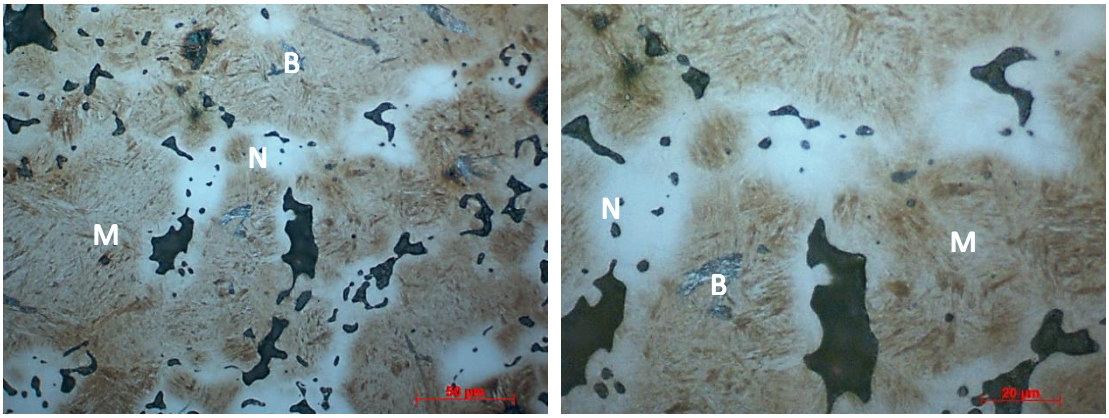

Figure 25 : Microstructure of DHP-T200 sample at different magnifications

DHP-T300

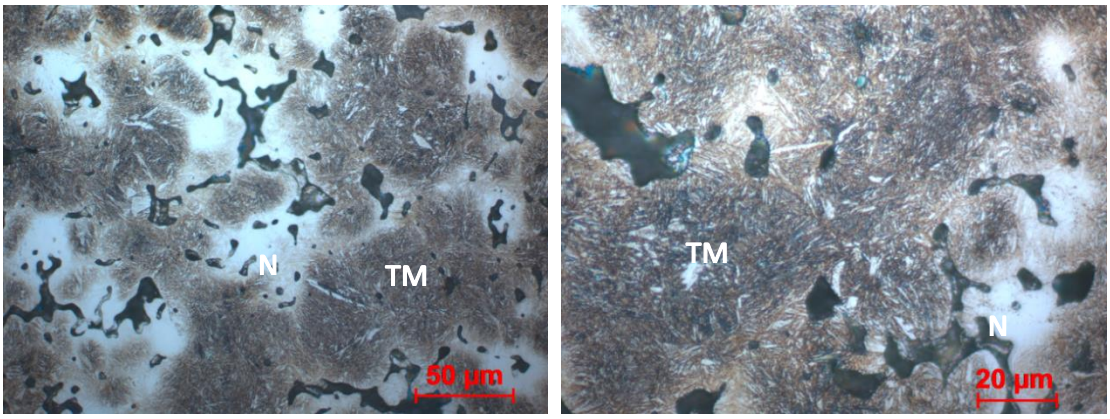

Figure 26 : Microstructure of DHP-T300 sample at different magnifications showing tempered martensite (TM)

DHP-DC-UT

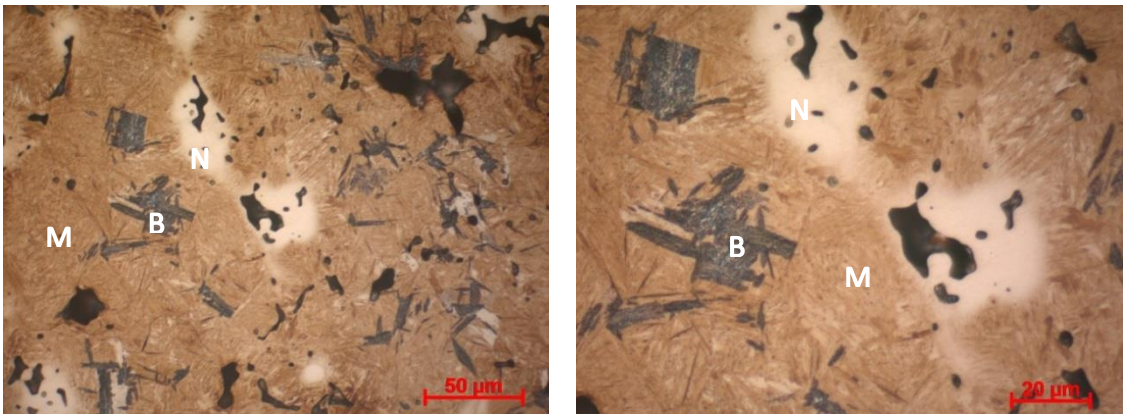

Figure 27 : Microstructure of DHP-DC-UT sample at different magnifications

DHP-DC-T200

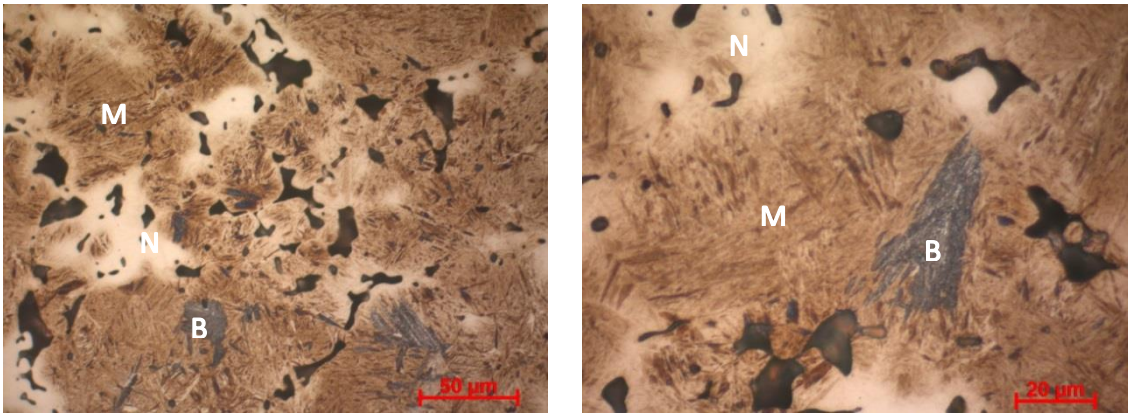

Figure 28 : Microstructure of DHP-DC-T200 sample at different magnifications

DHP-DC-T300

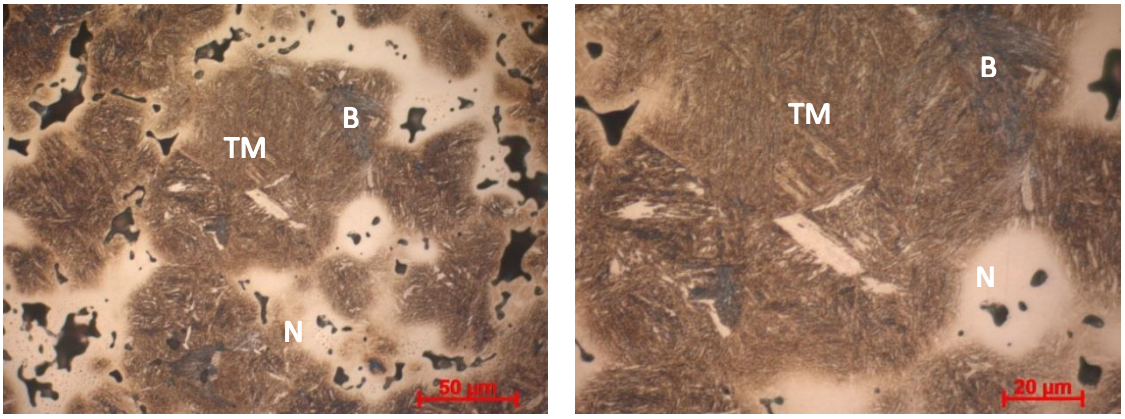

Figure 29 : Microstructure of DHP-DC-T200 sample at different magnifications showing tempered martensite (TM)

4.4 EDX Analysis

The SEM combined with EDX analysis was used to perform elemental mapping of the microstructure in order to understand which phases are present as well as the elemental distribution within them.

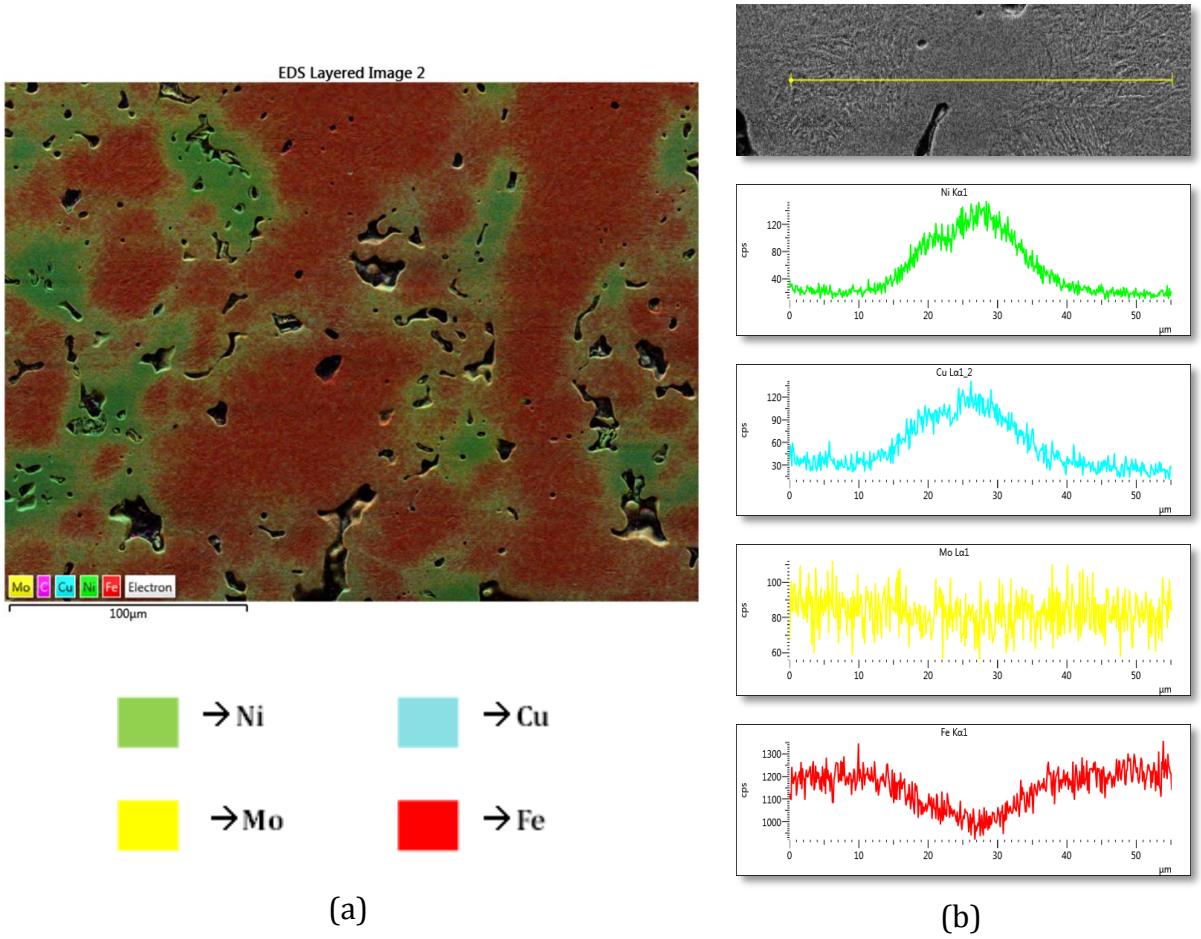

Figure 30 : (a) Elemental mapping from EDX analysis of DHP-T300 sample and (b) EDX line analysis

Figure 30 (a) shows the elemental mapping of DHP–T300 sample where green areas represent the Ni-rich austenite. EDX analysis confirms that these regions are rich in nickel and copper and it is also more evident from the line EDX analysis through the austenite region as shown in Figure 30 (b). The particle core consists of martensite which is composed preferably by Fe with presence of Mo and C distributed homogeneously in this system.

4.5 XRD Analysis

The measurement of the austenite content by XRD shows the total austenite content which is combination of Ni-rich austenite and retained austenite in martensite as both corresponds to the FCC phase. Table 10 shows measured fraction of the austenite in the different samples. In case of sinterhardened-tempered samples, the austenite content decreases with increasing tempering temperatures whereas the sinterhardened-deepcooled-tempered samples show a small amount of austenite (the values are close to the equipment's detection limit) as given in Table 10 and shown in Figure 31.

Table 10 : Residual austenite content of samples from XRD analysis

Samples	Austenite %
DHP - UT	14,7 ± 2,9
DHP - T200	12,7 ± 1,2
DHP - T300	8,0 ± 1,2
DHP - DC - UT	2,9 ± 1,6
DHP - DC - T200	2,4 ± 0,3
DHP – DC - T300	2,4 ± 0,9

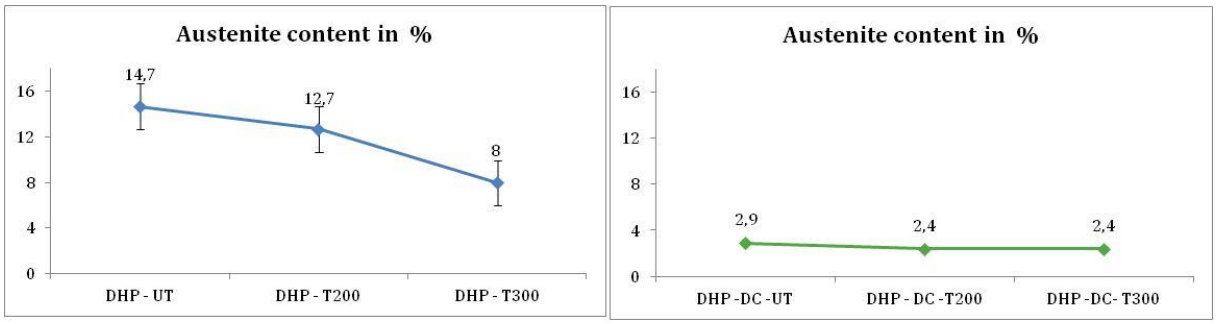

Figure 31 : Austenite content in the samples

Table 11 shows the austenite content measurement on the sinterhardened and sinterhardened-tempered (at 200 and 300°C) samples before and after creep test at carried out at 120°C for 1 million seconds. Results clearly indicate that there is no significant difference in austenite content before and after creep.

Table 11 : Austenite content measured before and after creep testing for 1 million seconds

Samples	Austenite %	
	before creep	after creep
DHP-UT	15,8±3,5	16,8±2,3
DHP-T200	12,7±1,2	11,6±1,4
DHP - T300	10,1±1,8	9,3 ± 1,8

Measurements of the residual austenite content were also performed on sinterhardened and sinterhardened-tempered specimens after heating of the samples at 120°C in a

furnace (in air) without any loading for 100 hours and 200 hours. This was done in order to see the effect of tempering for a long time at such a low temperature. However, results indicate that there is no significant change in the austenite content even after 200 hours, see Table 12.

Table 12 : Austenite content after tempering at 120°C for 100 and 200 hours without any load

Samples	Austenite %		
	as received	after 100 hours at 120°C	after 200 hours at 120°C
DHP-UT	13,7±5,7	14,6±1,8	12,5±2,5
DHP-T200	15,6±2,4	13,9±1,2	13,3±1,8
DHP-T300	10,7±1,5	10,1±1,7	-

4.6 Apparent Hardness

Apparent hardness is the macrohardness including the porosity effects on the microstructure. As sintered components in most practical cases contain porosity, it is important to take these into consideration as well. Overall hardness trend for the studied materials shows that the hardness is decreasing from the untempered to tempered samples, see Figure 32 .

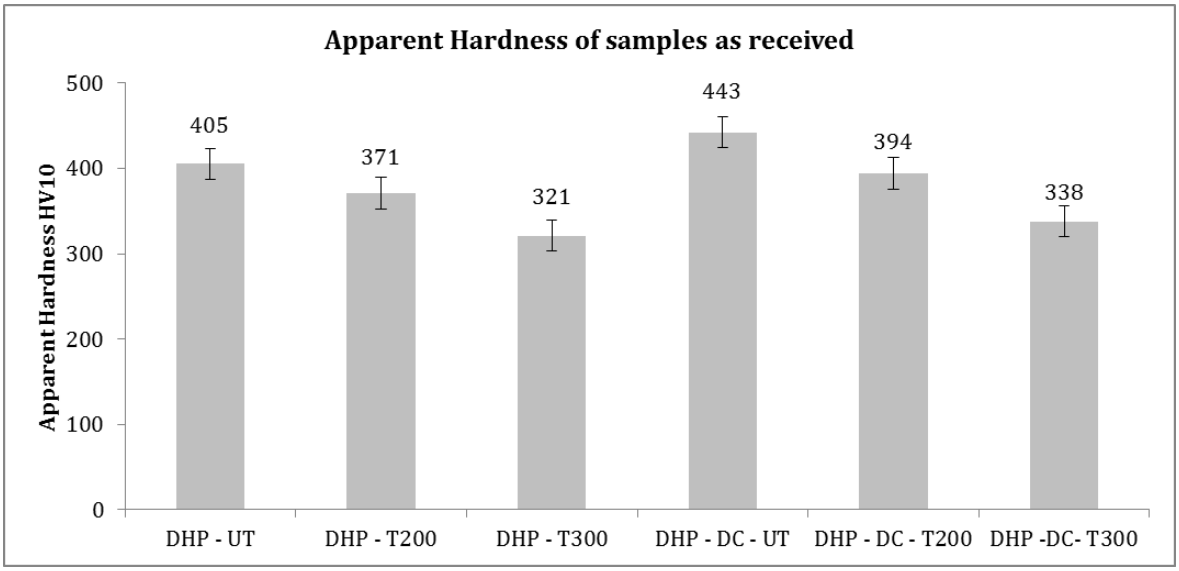

Figure 32 : Apparent hardness of the samples

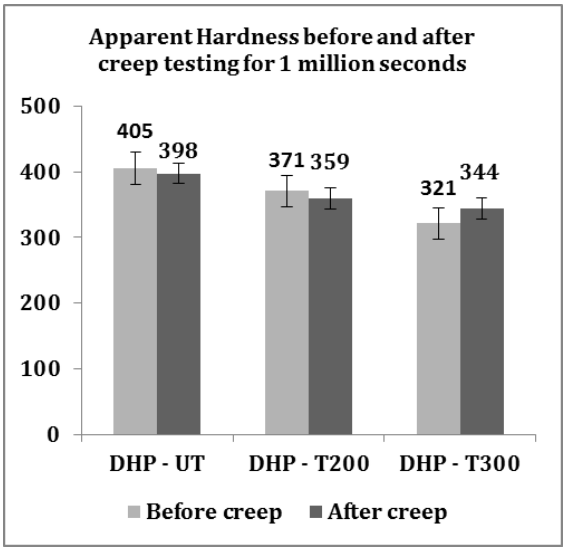

Figure 33 : Apparent hardness of the sinterhardened samples before and after creep

Hardness test on the samples after creep testing for 1 million seconds, see Figure 33, does not show any significant change in the hardness values. There is a slight decreasing trend in case of untempered and tempered at 200°C sample and slight increasing trend in case of tempered at 300°C samples, but all the changes are in the range of the experimental and measurement errors.

4.7 Microhardness

Initial studies on the different microstructures of the samples reveal that each phase has their typical hardness range. Martensite is the hardest and austenite having the lowest hardness among all the phases. Hence, accurate analysis of the microhardness of the different phase constituents in case of all materials was performed, see Figure 34.

a

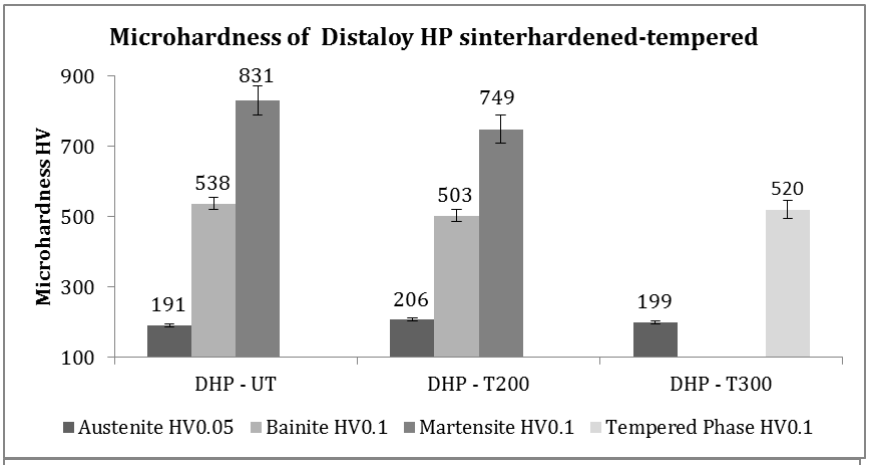

b

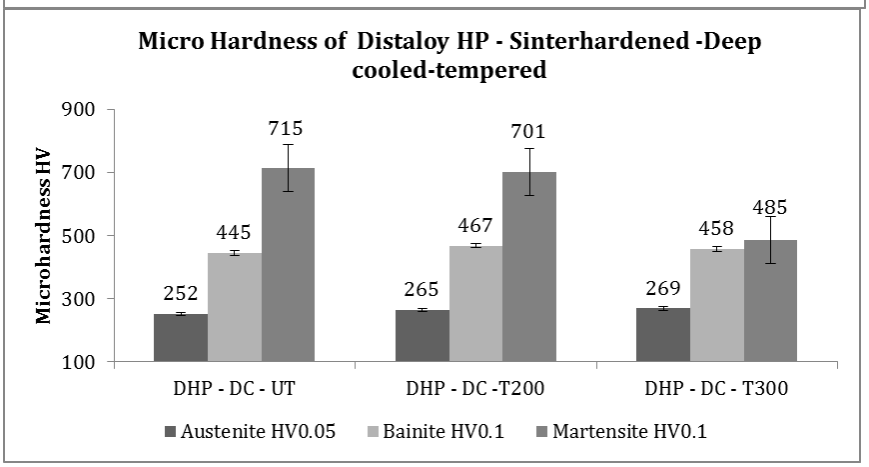

Figure 34: Microhardness of the sinterhardened–tempered samples (a) and sinterhardened-deepcooled–tempered specimens (b)

In case of sinterhardened–tempered samples, martensite hardness drops with increasing tempering temperature. Hence, after tempering at 300°C, the martensite (called tempered in further discussion) has the lowest hardness. The bainite hardness decreases from untempered to tempered (at 200°C) samples and there is no bainite observed in case of DHP-T300. Ni-rich austenite is present in all samples with similar hardness which reveals that this phase is stable throughout the entire tempering stages, as also confirmed its presence by metallography.

In case of deepcooled samples, the martensite hardness drops upon tempering similar to sinterhardened-tempered samples. It is important to note that the martensite hardness is significantly lower in case of deepcooled samples in all tempered conditions as comparison to similar materials after conventional sinterhardening-tempering, see Figure 34. Martensite hardness decreases with increasing tempering temperature

whereas the hardness of bainite retains at the same microhardness level even after tempering up to 300°C in case of deep-cooled samples. The Ni-rich austenite has comparatively higher hardness than in the sinterhardened-tempered samples and retains at that same level throughout the tempering stages.

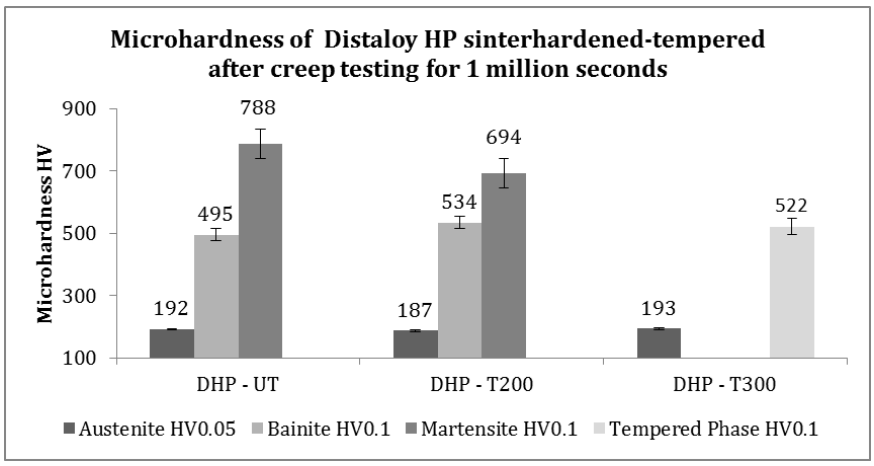

Figure 35 Microhardness of the samples after creep testing at 120°C for 1 million seconds (~ 277 hours)

The microhardness tests after creep testing for 1 million seconds on the sinterhardened–tempered samples indicating hardness decrease for the martensite. Significant drop in bainite hardness was observed after creep test in the untempered samples but the hardness was in the same level in case of DHP-T200 samples. In case of DHP-T300 before and after creep, there is no significant difference in terms of hardness change in the tempered martensitic phase. Microhardness of the Ni-rich austenite for all the samples before and after creep testing remains in the same level which confirms the high stability of this phase.

4.8 Creep

Based on the tensile results of the Distaloy HP material processed at different conditions, see Table 7, the minimum yield strength (Rp0.2 stress) among all the samples was considered for the loading for creep tests. The sinterhardened-untempered sample (DHP-UT) exhibits lowest yield stress and therefore 90% of its yield strength was chosen as the load for the creep test, which yields about 20 kN for the chosen specimen geometry. Hence, in order to keep consistency and to be able to compare the creep results, the constant load of 20 kN was applied in case of all specimens to perform creep testing for prolonged duration.

Table 13 : Yield strength equivalent to 20 kN equivalent of the corresponding samples, in %

Samples	20 kN equivalent of yield strength in %
DHP-UT	~90
DHP-T200	~80
DHP-T300	~75
DHP-DC-UT	
DHP-DC-T200	~63
DHP-DC-T300	~73

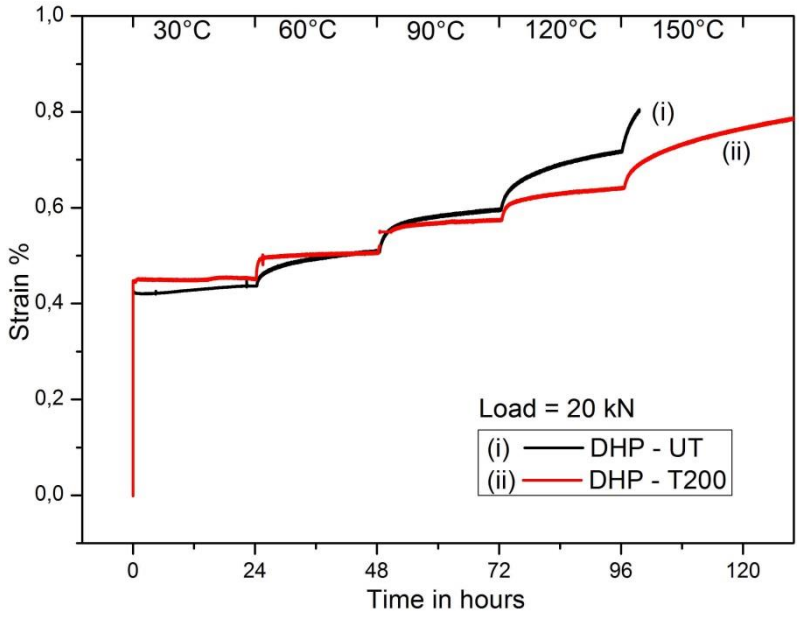

Figure 36 : Creep test curves for DHP- UT and DHP- T200. Strain (%) vs. time (hours), carried at constant load of 20 kN at varying temperatures from 30 to 150°C at an interval of 24 hours holding at different temperatures.

In order to study the influence of temperature at a constant load, a short term (24 hrs) creep test at different temperatures was carried out. Figure 36 shows the creep testing of DHP-UT and DHP-T200 at different temperatures with 30°C increments for

approximately 24 hrs of duration. It is clearly seen that in case of DHP-UT at 30°C the strain rate is almost negligible. With increasing intervals from 60°C and above, there is an increase in strain up to 90°C and rapid increase in strain at 120°C onwards. Similar behaviour in case of DHP–T200 was observed, also indicating rapid increase of strain rate at 120°C, see Figure 36.

The cyclic creep curve of deepcooled and tempered material DHP-DC-T200 tested at 20 kN load, see Figure 37, indicate that the deepcooled material is rather stable up to 90°C. Noticeable change in strain rate was observed at 120°C and indicate increasing trend with increasing temperature.

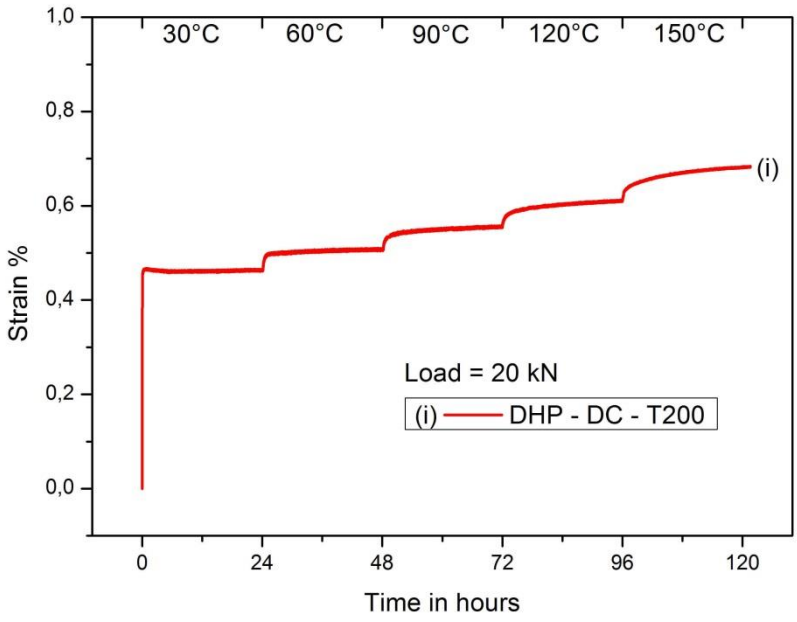

Figure 37 : Creep test curve for DHP-DC-T200, strain (%) vs. time (hours), carried at constant load of 20 kN at varying temperatures from 30 to 150°C at an interval of 24 hours holding at different temperatures

Based on the results from the short-term creep testing at different temperatures, it was decided to perform the long-term creep tests on the samples at a constant temperature of 120°C and at a constant load of 20 kN.

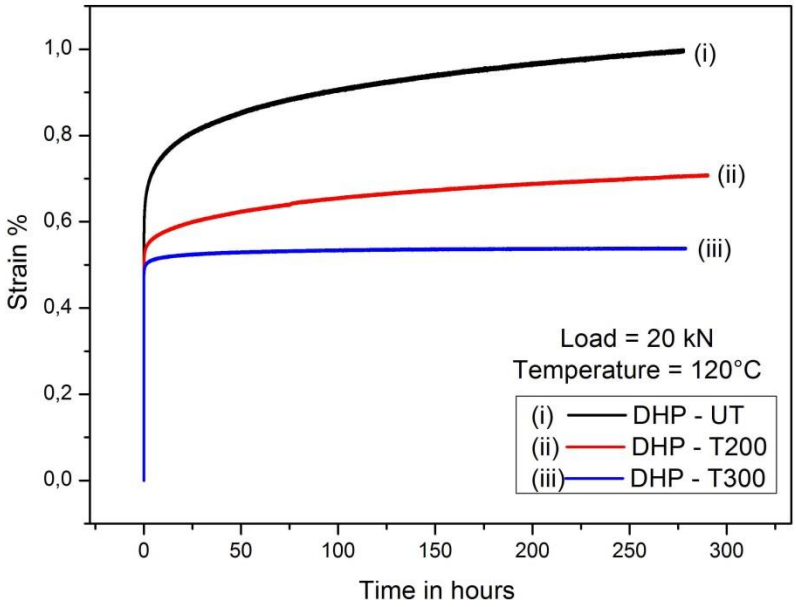

Figure 38 : Creep curves for Distaloy HP samples carried out at constant load of 20 kN at 120°C for ~ 277 hours (1 million seconds)

Figure 38 shows strain vs. time plots of the sinterhardened–tempered samples DHP-UT, DHP-T200 and DHP-T300 from the prolonged creep testing performed at a constant load of 20 kN at 120°C. All the samples exhibit the initial stage of creep i.e. primary or transient creep. The initial increase of strain upon loading until maximum load is constant which is also termed as an instantaneous strain DHP-UT samples exhibit primary creep stage for up to 20-25 hours and then reach the secondary stage of creep where the strain rate is steadily increasing. DHP-T200 samples passes the primary creep at an early period of time and reach secondary creep stage at a faster rate and further maintain constant strain rate at this stage. DHP-T200 has a lower strain rate during secondary stage of creep as compared to the untempered sample (DHP-UT). In case of the DHP-T300 sample, tempered at higher temperature, it possesses the lowest change in strain. It is stable even up to 1 million seconds (~277 hours) at 120°C. Thus the temperature and chosen load has a minor influence for the tempered material at higher temperature.

In case of sinterhardened–deepcooled samples, the creep testing was performed only for the tempered samples due to the extremely brittle nature of the deepcooled-untempered samples (DHP-UT they fail before it reaches the maximum load). The strain vs. time creep curves for DHP-DC-T200 and DHP-DC-T300 shows a negligible amount of strain rate when compared to the sinterhardened–tempered samples tested under the similar load conditions at 120°C until 100 hours (~3.6 x 10^5 seconds), see Figure 39. DHP-DC-T200 creep curve shows lower amount of initial creep and also the strain rate is comparatively lower than DHP-DC-T300.

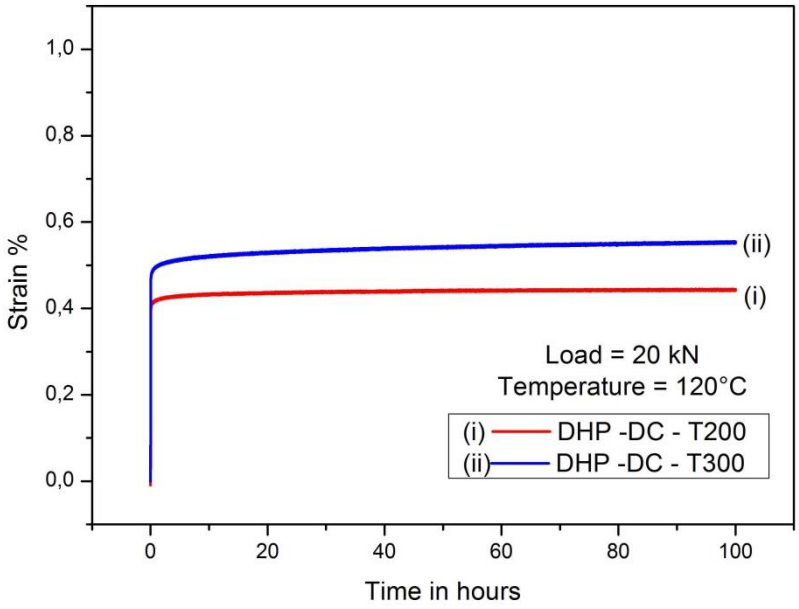

Figure 39 : Creep curves for Distaloy HP deepcooled samples carried at constant load of 20 kN at 120°C for 100 hours (~ 3.6 x10^5 seconds)

In case of sinterhardened-tempered samples, see Figure 38, higher tempering temperature lead to better creep resistance, whereas in case of deepcooled samples, see Figure 39, there is no effect of tempering temperature on the creep behaviour. This might be due to the yield strength of the material, as DHP-DC-T200 exhibits much higher yield strength as compared to DHP-DC-T300 material, see Figure 13.

Table 14 : Strain rate from secondary creep (steady state creep) stage of the samples creep tested at 120°C and 20 kN for the curves in Figure 38 and Figure 39

Samples	Strain rate (s^{-1})
DHP-UT	1.50 x 10^{-7}
DHP-T200	0.83 x 10^{-7}
DHP-T300	0.07 x 10^{-7}
DHP-DC-UT	*
DHP-DC-T200	0.31 x 10^{-7}
DHP-DC-T300	0.54 x 10^{-7}

*** It is too brittle**

DHP-UT samples exhibits higher strain rate in the secondary creep stage when compared to all other samples, as seen in Table 14.

As the low temperature creep obeys logarithmic dependence of strain vs. time, the creep curves in case of deep cooled samples DHP-DC-T200 and DHP-DC-T300 were fitted based on the equation (1) in chapter 2.2.2 up to 100 hours. Curves were further extrapolated up to ~277 hours (1 million seconds) to define the steady state creep behaviour, see Figure 40.

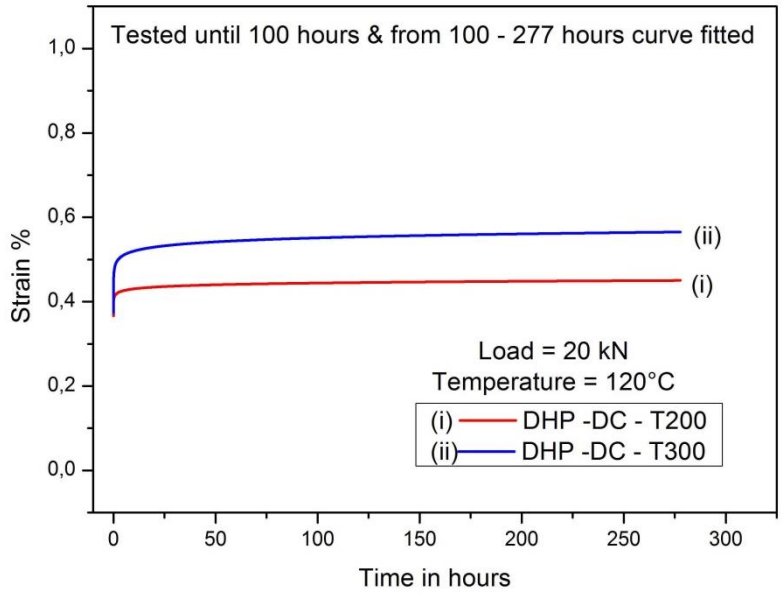

Figure 40 : Creep curves for Distaloy HP deepcooled samples carried out at a constant load of 20 kN at 120°C for 100 hours (~ 3.6 x10^5 seconds) and extrapolated modelled up to ~ 277 hours (1 million seconds)

Additionally creep tests were performed for different samples for a limited period of time at different loads, corresponding to 90% of the respective yield strength of the tested materials, to observe the influence of stress level. In the case DHP-T200 and DHP-T300, 90% of the material yield strength is equivalent to 24 and 24.5 kN, respectively. It can be observed that the instantaneous strain increased for DHP-T200 and DHP-T300 which is due to increased load from considered before (20 kN), see Figure 41. Also, based on the limited data from Figure 41 the steady state creep for all the samples was extrapolated up to ~300 hrs see Figure 42 and its maintains the constant strain rate.

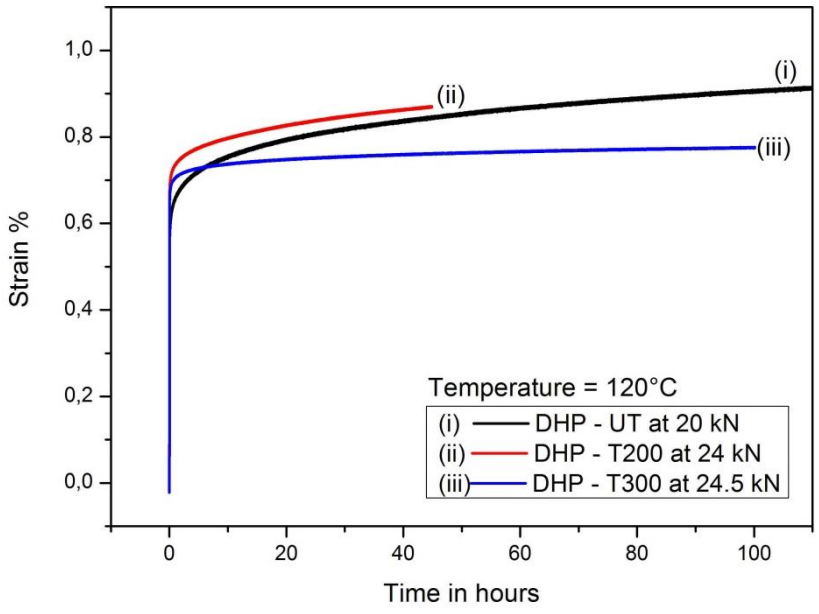

Figure 41 : Creep curves for Distaloy HP samples after different tempering carried out at load equivalent to 90% of their respective yield strength (Rp0.2) at 120°C

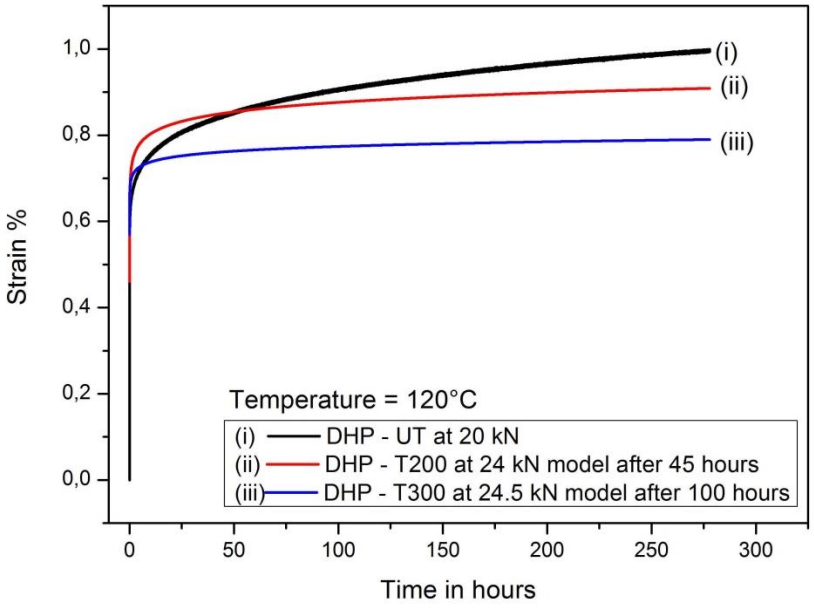

Figure 42 : Creep curves for Distaloy HP samples after different tempering carried out at load equivalent to 90% of their respective yield strength (Rp0.2) at 120°C. Creep curves for both DHP – T200 and T300 are extrapolated up to 300 hours

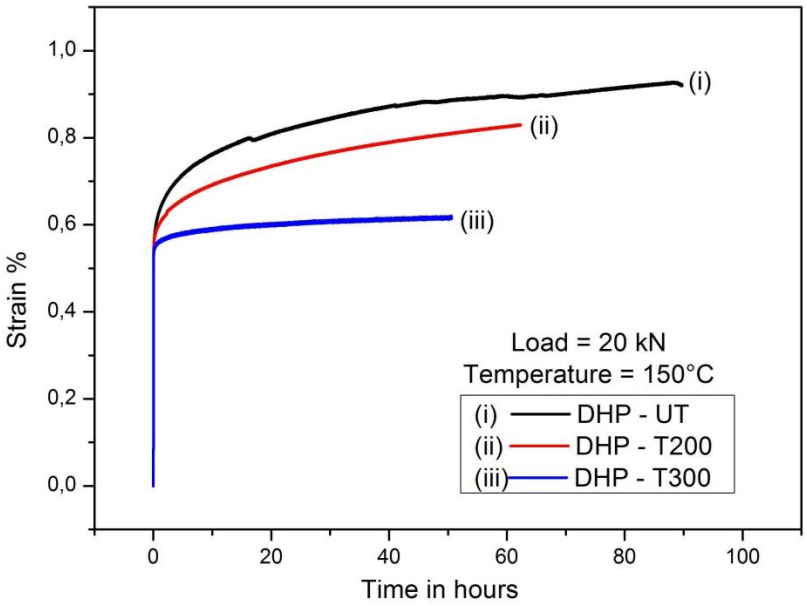

Figure 43 : Creep curves for Distaloy HP samples carried out at constant load of 20 kN at 150°C

Creep tests were also performed at constant load of 20 kN and at higher temperature of 150°C, see Figure 43. It can be observed that the creep curve of DHP-UT is not as smooth as compared to two other curves. There is a decrease in strain rate after about 40 hrs. It is possibly due to the tempering effect – temperature (150°C) combined with load which is high enough to initiate the tempering effect of untempered DHP samples.

4.8.1 Strain value measurements (Dimensional change)

Strain value in the creep experiments were obtained from extensometer and the total strain change is too small to measure in terms of geometrical dimensions (thickness and width) of the samples before and after creep. Hence, 10 hardness indents were made on the polished samples before creep measurement and the distance between each indents were measured before and after creep experiments using optical microscope, see Figure 44 and Figure 45. This is performed in order to validate the strain associated with the creep testing.

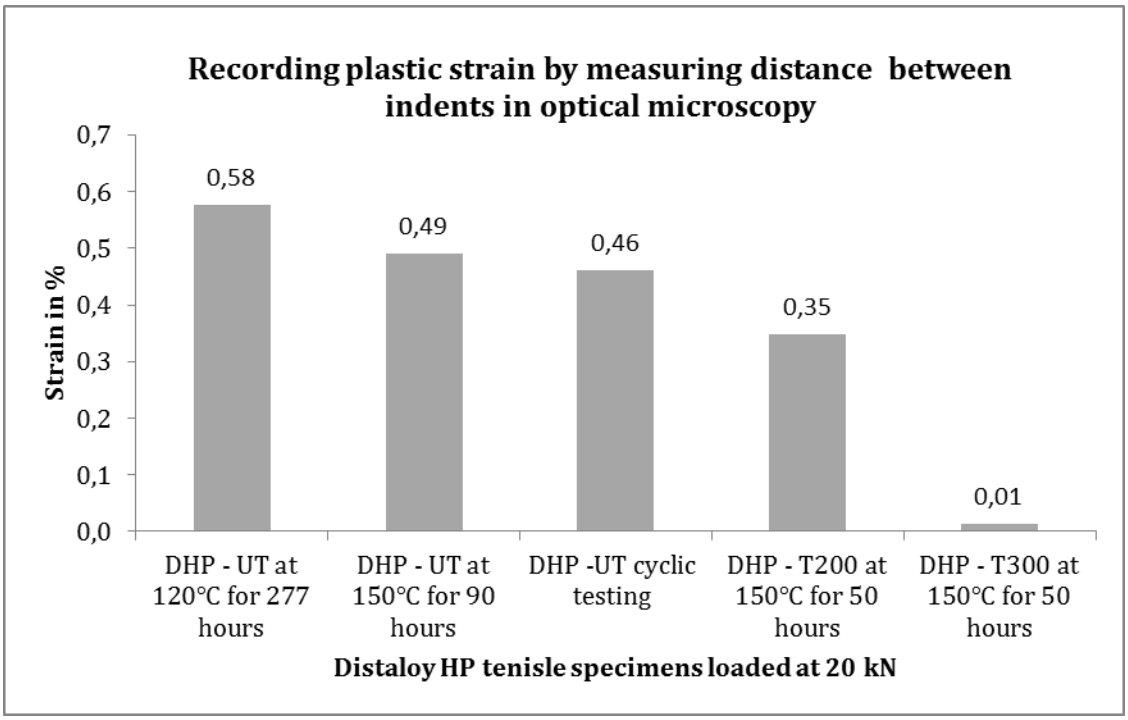

Figure 44 : Measured plastic strain of different samples after creep tests at different temperatures and times, carried out by measurement of distance between the indents using optical microscope

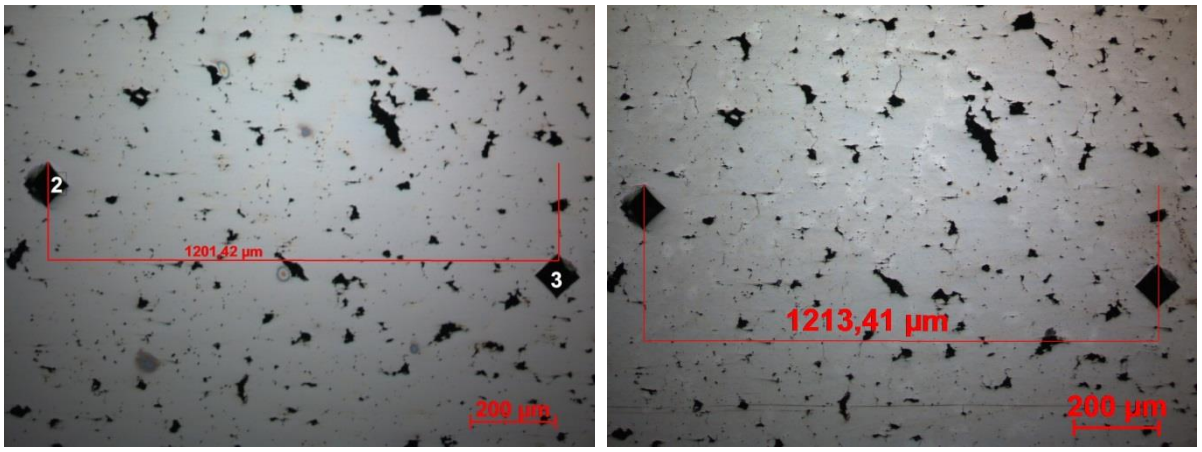

Before creep After creep

Figure 45 : Indent measurements of DHP-UT before and after creep test for 1 million seconds

5 Discussion

Number of characterisation techniques was applied in order to determine the material microstructure and its properties before and after creep tests in order to understand the initial material characteristics and changes observed after creep testing.

5.1 Distaloy HP Material Characteristics

Distaloy HP exhibits its prevalent heterogonous microstructure as a result of diffusion bonded Ni and Cu as explained in chapter 4.3. In case of DHP-UT upon sinterhardening, the microstructure consists of predominantly martensitic structure with bainite regions and Ni-rich regions surrounding the pores. During sinterhardening, supersaturated austenite is cooled from high temperature to low temperature. Diffusionless transformation takes place while cooling that forms low density phase, martensite, which results in volume expansion that induces high internal stresses [32]. This is evident from the hardness values of the DHP-UT samples, both the apparent hardness and the microhardness of the martensite phase (see Figure 32 and Figure 34). Martensitic phase contributes significantly to the overall hardness of the material. The fractography of DHP-UT samples (see Figure 17) show transgranular cleavage and decohesion facets typical of the brittle failure correspond to the martensitic structure.

Upon tempering, the internal stresses owing to the martensitic transformation are relieved and the stored free energy is reduced [32]. As the result, the DHP-T200 samples exhibit improved ductility and tensile strength (see Table 7) with a drop in martensite hardness. This contributes to the overall drop in apparent hardness (see Figure 32 and Figure 34:). The fractography (see Figure 18) shows that the DHP-T200 samples are characterised by the transparticle ductile fracture with deep dimples, which is characteristic for high mechanical properties.

The tempering of martensite at 300°C results in precipitation of carbides out of the martensite plates. Hence, tempered martensite is characterised by drop in hardness but improved toughness of the material that is evident from the higher yield stress (Rp0.2 stress) of the material (see Figure 13). In general there is a significant drop in the hardness of martensite upon tempering from 200°C to 300°C due to the fact that it is a tempered martensite as compared to the prior stages. This compensates for the better properties obtained upon high temperature tempering.

The diffusion bonded Ni and Cu, which are FCC stabilizing elements, form Ni-rich regions. These appear as white areas seen in the microstructure surrounding predominantly at the interparticle boundaries and pore regions, due to the slow diffusivity of Ni into Fe as compared to Fe into Ni. It is evident from the EDX line analysis (see Figure 30) that these areas are rich in nickel and stable even upon tempering up to 300°C (see Figure 26) and microhardness values (see Figure 34:) of approximately 190 to 200 HV0.05 throughout the tempering stages. Even after the creep testing at 120°C

for 1 million seconds (see Figure 35), there is negligible change in the hardness of Ni-rich regions, implying that it is very stable under such conditions.

The XRD measurements on these samples reveal that the amount of austenite (from FCC peaks) is the combination of Ni-rich regions and retained austenite. Table 10 shows clearly that the amount of austenite content decreases upon tempering. Based on the microstructural investigation and the theoretical considerations, it is plausible that the retained austenite entrapped between the martensitic plates is transformed. As the retained austenite is not stable at room temperature, upon tempering, it decomposes in to ferrite and carbides. It is also clear from the XRD measurements carried on deepcooled samples that the retained austenite was assumed to transform completely into martensite. As a result, the apparent hardness of the deepcooled samples is increased upon quenching when compared to the as sinterhardened-tempered samples (DHP-UT, DHP-T200 and DHP-T300) due to increased martensite content as a result of retained austenite transformation (see Figure 32). The increase in apparent hardness is also contributed by the higher microhardness value of Ni-rich regions which increases by ~70 HV0.05. Austenite content measurement on deepcooled samples shows that there is no change in the austenite content upon tempering since there is no retained austenite left as a result of deepcooling.

Further detailed investigation of retained austenite is necessary, since the measured content after deepcooling is close to the equipment's detection limit. There is no defined yield point for deepcooled untempered samples as they fractured before yielding as revealed from the tensile results. The fracture surface shows large amount of decohesion and cleavage facets (see Figure 20). A slight increase is observed in percentage elongation upon tempering at 200°C and 300°C (see Figure 13), with increase in yield strength (Rp0.2) in case of DHP-DC-T200. This is attributed to the stress-relieved martensitic microstructure. Whereas, the DHP-DC-T300 samples show similar behaviour as the DHP-T300 samples with no significant difference in terms of yield and ultimate tensile strength. The microstructure of DHP-DC-T300 samples reveals well-tempered martensite with carbide precipitates. This results in hardness drop of ~200HV0.1. Nevertheless, deepcooled tempered samples DHP-DC-T200 and DHP-DC-T300 has limited elongation in comparison with DHP-T200 and DHP-T300 samples. This is also evident from the fracture surface that the deepcooled specimens exhibit cleavage and quasi cleavage facets typical of a brittle failure.

From the basic characterisation of the samples, it is found that the sinterhardened-tempered samples have a stable microstructure and are characterised by high tensile strength and possess enough ductility which contributes to high toughness of the material, suitable for high performance applications. At the same time, sinterhardened–deepcooled-tempered samples comprise a higher fraction of martensite that is characterised by high internal stresses which exhibits higher yield strength but fails predominantly in brittle manner as observed from the fractography.

5.2 Creep

Low temperature creep is characterised by only two stages of creep (see Figure 38) as compared to the three creep stages characteristic for high temperature creep. Primary creep upon initial loading after it reaches the instantaneous strain it maintains steady state throughout the entire period in all the three samples and there is no third stage that leads to failure. Comparison of the tensile strain from the tensile testing results after yield limit (see Figure 13) with the amount of strain in creep testing after the instantaneous strain (see Figure 38) until 1 million seconds (in steady state), reveals the strain after creep is much lower. Even though along with 20 kN constant load, the temperature activation is involved.

The creep testing of deep cooled-tempered samples, DHP-DC-T200 (see Figure 39) shows very low strain compared to the DHP-DC-T300. This is due to the high yield strength of the DHP-DC-T200 and the applied load of 20 kN (see Table 13) corresponds to around 60% whereas for DHP-DC-T300 it is around 70% of its yield stress. Even though DHP-DC-T300 consists of tempered microstructure, the DHP-DC-T200 has higher strength. This steady behaviour of both the deepcooled-tempered samples is due to the complete transformation of retained austenite after deep cooling and tempering of martensite. By considering , the tensile strain from the tensile testing results after yield limit (see Figure 13), the amount of strain after yielding for the sample to reach failure in tensile testing and the amount of strain in creep testing after the instantaneous strain (see Figure 38) until 1 million seconds(in steady state) is too low during creep.

Low temperature creep curves obey logarithmic creep law as clearly seen on deep cooled samples, hence a model has been developed and fitted for 300 hours by using 100 hours of experimental data (see Figure 40). Also the constant load of 20 kN used for the creep testing for all the samples (see Table 13) is not equivalent with respect to their strength, but in actual conditions a constant load can be applied irrespective of the sample conditions.

5.3 Factors influencing creep

The factors influencing the creep behaviour at low temperatures are discussed below based on the experiments on the DHP sinterhardened samples.

5.3.1 Microstructure influence

From the different samples, it is clearly observed that the tempered samples DHP-T200 and DHP-T300 exhibit lower creep strain as compared to the untempered DHP samples. The sinterhardened microstructure consists of initial martensite, transformed from austenite with high internal stresses and retained austenite between the martensitic plates. Upon tempering, internal stresses are relieved and free energy is reduced by precipitation of transition carbides. At higher tempering temperatures, the retained austenite is transformed into ferrite and carbides. The tempered microstructure is free

of internal stresses and retained austenite which makes the microstructure more stable than the untempered microstructure DHP-UT. This is shown in Figure 46 where the strain rate is decreasing with tempering.

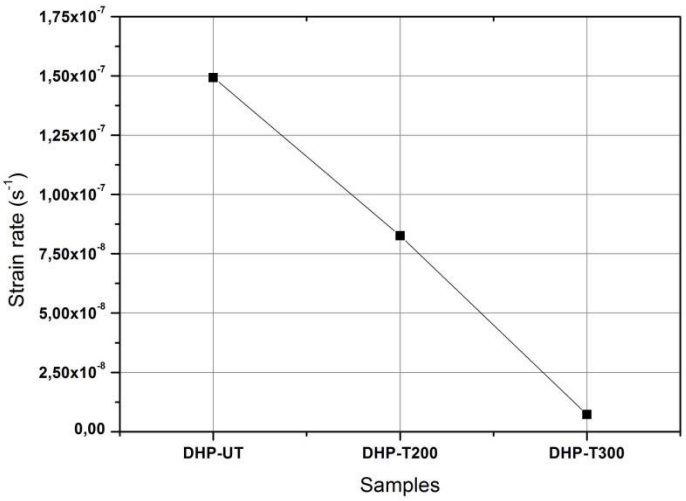

Figure 46 : Strain rate dependence on tempering condition for different tempered samples, creeped for 1 million seconds

5.3.2 Temperature influence

Temperature activation seems to be the most important factor determining creep behaviour. It is evident from the short-term creep experiments at different temperatures in Figure 36 and Figure 37 as well as high temperature creep experiments at 150°C see Figure 43 that there is a significant increase in creep rate with increasing temperature.

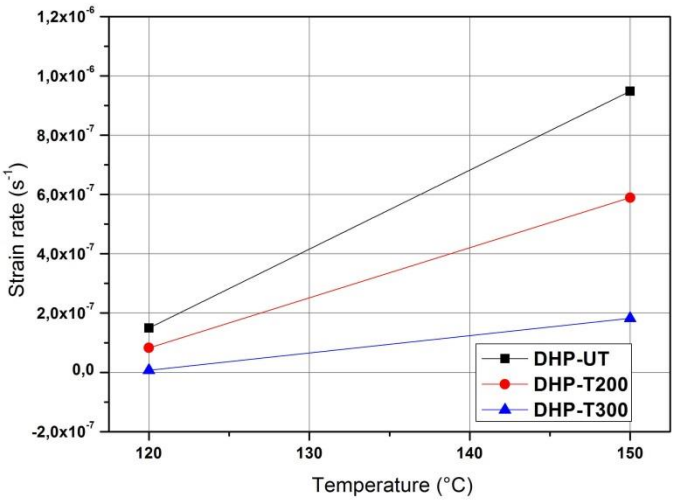

Figure 47: Strain rate dependence on tempering conditions showing the temperature influence on creep

The cyclic creep tests of the DHP-UT and DHP-T200 show that there is negligible strain at room temperature and the strain value increases with temperature at 90-120°C. The change is more prominent as a result of thermal activation along with loading. DHP-T200 exhibits low strain rate values at intermediate temperature when compare to the untempered sample. This is due to the stability of the DHP-T200 microstructure due to the tempering. In case of DHP-DC-T200 sample, the change is dominant only above 120°C and in overall much less change in strain compared to the only sinterhardened-tempered sample. Figure 47 summarise the results of mentioned creep experiments at different temperatures and shows the increasing strain rate with increasing the testing temperature. Corresponding creep curves can be found in Appendix 3.

5.3.3 Stress influence (Loading conditions)

Different loading conditions will influence the creep behaviour see Figure 10. Increase in stress introduces more dislocations and strain hardening during the initial stage of creep that further change creep behaviour accordingly. As it is evident from creep results (see Figure 48) the increasing stress from 20 to 24 kN in case of DHP-T200 increases the creep strain and. the increasing strain rate with increasing the loading conditions for other specimens as well. Corresponding creep curves can be found in Appendix 3.

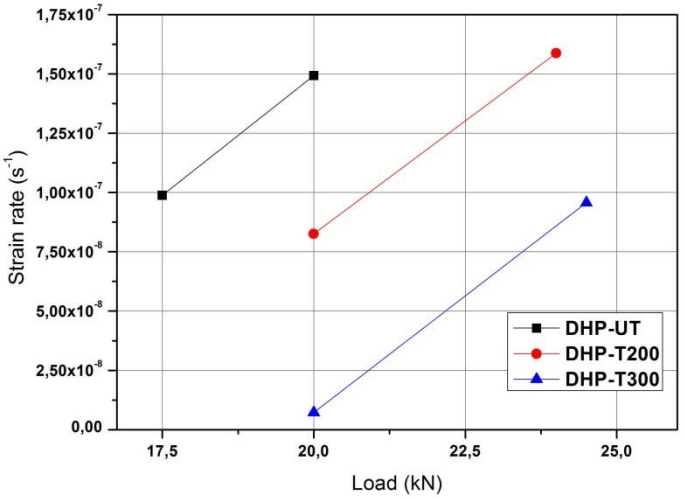

Figure 48: Strain rate dependence on stress applied for different tempered samples showing its effect on creep.

6 Summary

- Creep is observed in PM steels at low temperatures (i.e. $T/T_m<0.3$) under high static load conditions.

- Sinterhardened–untempered (DHP-UT) samples exhibits higher strain values than the tempered samples due to unstable microstructure (martensite and retained austenite).

- Sinterhardened-tempered at 300°C (DHP-T300) samples exhibits lower creep strain due to the tempered microstructure.

- Tempering at high temperatures improves the structural stability of sinterhardened PM steels which can be suitable for high performance applications.

- Ni-rich austenite is a phase characterised by high stability in studied materials which, however, doesn't have any influence on the dimensional stability of the sample even after creep testing at 120°C for sustained time period.

- The retained austenite is eliminated in deep cooled samples, and the deep cooled samples tempered at 200 and 300°C exhibit negligible amount of creep strain. This can be attributed to the absence of retained austenite and also the amount of load that has been applied in creep testing which corresponds to 60 – 70 % of the yield stress of this material.

- Deepcooled samples are too brittle for high performance applications and extreme measures should be taken by considering the geometry and the type of loading when used in actual applications.

- Among the creep influencing factors, the temperature influence is dominant on creep behaviour in comparison with other factors.

7 Future work

- It is important to clarify the influence of temperature and stress on Ni-rich regions.

- Alternative method for retained austenite content estimation has to be performed.

- Simulation of the similar conditions in case of materials with more homogenous microstructure and without Ni-rich regions has to be performed. (e.g. CrM: Cr prealloyed powder grade).
- Creep tests under compression can be performed to observe the creep behaviour with similar condition in order to compare and understand the deformation mechanism in PM steel components.

- Detailed microstructural investigation of martensite and retained austenite transformation has to be performed by dilatometry studies.

- In order to observe the influence of porosity, creep tests have to be performed on fully densified samples (produced by e.g. Hot Isostatic Pressing (HIP)) with similar composition.

- A mathematical model has to be developed to be able to predict the creep behaviour in PM steels.

8 Acknowledgement

First, I would like to thank my examiner Associate Professor Eduard Hryha for the guidance, and the opportunity to work on this project and I would like to thank my supervisors Dr.Kumar Babu Surreddi and Dr.Henrik Karlsson (Volvo AB) for their extended support and guidance. I would like to thank Volvo AB and Höganäs AB for the project contribution. I would like to thank other people in this project group; Professor Lars Nyborg, Head of the department for his support, Dr.Michael Andersson (Höganäs AB) for his guidance and the support with the samples and Gunnar Åkerström for his support with the testing at Volvo.

Also, I would like to thank Seshendra Karamchedu, Assoc. Prof. Johan Ahlström, Seyed B. Hosseini and Dr.Eric Tam at the Department of Materials and Manufacturing Technology, Chalmers University of Technology for all their support with equipments and fruitful discussions during the course of my thesis.

Apart from that, I would like to thank all colleagues at the Department of Materials and Manufacturing technology, Chalmers University of Technology and Materials Technology, Volvo Group Trucks Technology for their continuous support and guidance.

A special thanks to my grandparents and my parents, and my friends for their continuous support during my entire stay in Sweden.

9 References

[1] P. V. Morra, "Thermo-mechanical loading response of hardened and tempered iron-carbon based alloys," Ph.D.Thesis, Delft University of Technology, 2004.

[2] M.-N. Tan, "Micro-Creep of Hardened Bearing Steels Studied with Dilatometry," Chalmers University of technology, 2006.

[3] J. Nyqvist and J. Sandahl, "The Influence of Low Temperature Creep and Hydrogen in Hardened Bearing Steels," Chalmers University of Technology, 2007.

[4] H. D. Chandler, "Transient creep in mild steel and copper at room temperature," *Acta Metall.*, vol. 33, no. 5, pp. 835–840, May 1985.

[5] K. R. Williams and M. Taylor, "Creep of Mild Steel at Low Temperatures," *Mech. Mater.*, vol. 3, no. 1, pp. 1–10, 1984.

[6] C. Liu, P. Liu, Z. Zhao, and D. O. Northwood, "Room temperature creep of a high strength steel," *Mater. Des.*, vol. 22, no. 4, pp. 325–328, Jun. 2001.

[7] V. Sanchez-Galvez and M. Elices, "The relationship between tensile strain, creep and stress relaxation in cold-drawn steels at low temperatures," *Mater. Sci. Eng.*, vol. 78, no. 1, pp. 1–8, 1986.

[8] S.-H. Wang, Y. Zhang, and W. Chen, "Room temperature creep and strain-rate-dependent stress-strain behavior of pipeline steels," *J. Mater. Sci.*, vol. 36, no. 8, pp. 1931–1938, 2001.

[9] L. Zhang, H. Xu, Q. Ma, and Z. Wang, "Low-Temperature Creep Behavior of Commercially Pure Titanium TA2," *Rare Met. Mater. Eng.*, vol. 37, no. 12, pp. 2114–2117, 2008.

[10] H. J. Frost and M. F. Ashby, *Deformation Mechanism Maps:The Plasticity and Creep of Metals and Ceramics*. Pergamon Press, 1982.

[11] R. M. German, *Powder Metallurgy of Iron and Steel*. Wiley-Interscience, 1998.

[12] P. Ramakrishnan, "History of powder metallurgy," *Indian J. Hist. Sci.*, vol. 18, no. 1, pp. 109–114, 1983.

[13] G. S. Upadhyaya, *Powder metallurgy technology*. Cambridge Int Science Publ, 1997.

[14] W. Schatt and K. P. Wieters, *Powder Metallurgy Processing and Materials*. European Powder Metallurgy Association(EPMA), 1997, p. 492.

[15] M. Bulger, "State of the PM Industry in North America-2013," *Int. J. powder Metall.*, vol. 49, no. 3, pp. 29–32, 2013.

[16] M. Bulger, “State of the PM Industry in North America-2012,” *Int. J. Powder Metall.*, vol. 48, no. 4, pp. 29–32, 2012.

[17] B. Bergquist, “Statistical approaches to PM steel process improvements,” Linköpings Universitet, 1999.

[18] *Höganas Handbook for Sintered Components 1-6*. Höganäs: Höganäs AB, 2004.

[19] S. Karamchedu, “Delubrication of Chromium Prealloyed Powder Metallurgy Steels,” Chalmers University of Technology, 2013.

[20] W. B. James, “What is Sinter-Hardening?,” in *International Conference on Powder Metallurgy & Particlulate Materials PM2TEC*, 1998, vol. 98, pp. 55–60.

[21] W. B. James, “Recent developments in ferrous powder metallurgy alloys,” *Int. J. Powder Metall.*, vol. 30, no. 2, pp. 157–164, 1994.

[22] B. Lindsley and T. Murphy, “Dimensional precision in sinter-hardening PM steels,” *Mater. Sci. forum*, vol. 4808, pp. 1–4, 2007.

[23] E. Dudrová and M. Kabátová, “Fractography of Sintered Iron and Steels,” *Powder Metall. Prog.*, vol. 8, no. 2, pp. 59–75, 2008.

[24] M. A. Meyers and K. K. Chawla, *Mechanical Behavior of Materials*, 2nd ed. Cambridge University Press, 2009.

[25] M. E. Kassner and M.-T. Pérez-Prado, “Fundamentals of Creep in Metals and Alloys,” Oxford: Elsevier Science Ltd, 2004.

[26] G. E. Dieter, *Mechanical Metallurgy*, 3rd ed. New York: McGraw-Hill Book Company, 1986, p. 751.

[27] L. B. Getsov, “Low-temperature creep and stress relaxation in some materials,” *Met. Sci. Heat Treat.*, vol. 13, no. 3, pp. 250–251, 1971.

[28] R. Neu and H. Sehitoglu, “Low-temperature creep of a carburized steel,” *Metall. Mater. Trans. A*, vol. 23, no. September, pp. 2619–2624, 1992.

[29] A. Oehlert and A. Atrens, “Room temperature creep of high strength steels,” *Acta Metall. Mater.*, vol. 42, no. 5, pp. 1493–1508, 1994.

[30] U. H. Kivisäkk and E. Wallin, “Results from low temperature creep and relaxation experiments of four different stainless steels,” *Corros. 2008*, no. 08487, pp. 1–11, 2008.

[31] P. V. Morra, S. Radelaar, M. Yandouzi, J. Chen, and a. J. Böttger, “Precipitate coarsening-induced plasticity: Low temperature creep behaviour of tempered SAE 52100,” *Int. J. Plast.*, vol. 25, no. 12, pp. 2331–2348, Dec. 2009.

[32] H. Bhadeshia and R. Honeycombe, *Steels - Microstructure and Properties (3rd Edition)*. Elsevier.

[33] D. A. Porter, K. E. Easterling, and M. Y. Sherif, *Phase Transformations in Metals and Alloys*, 3rd ed. CRC Press, Taylor and Francis Group, 2009, p. 500.

[34] G. Speich and J. Breedis, "Martensitic Structures," *ASM Handbook.*, vol. 9, no. Metallograhy and Microstructures, pp. 165–178, 1985.

[35] S. Tekeli, A. Güral, and M. Gürü, "Influence of Tempering Temperature and Microstructure on Wear Properties of Low Alloy PM Steel with 1-2 % Ni Addition," *Mater. Sci. Forum*, vol. 534–536, pp. 629–632, 2007.

[36] F. Chagnon, M. Gagné, and R. T. Iron, "Effect Of Tempering Temperature On Mechanical Properties And Microstructure Of Sinter Hardened Materials," *Adv. Powder Metall. Part. Mater.*, vol. 2, 1999.

[37] *Standard Test Methods for Metal Powders and Powder Metallurgy Products*.

10 Appendices

10.1 Appendix 1

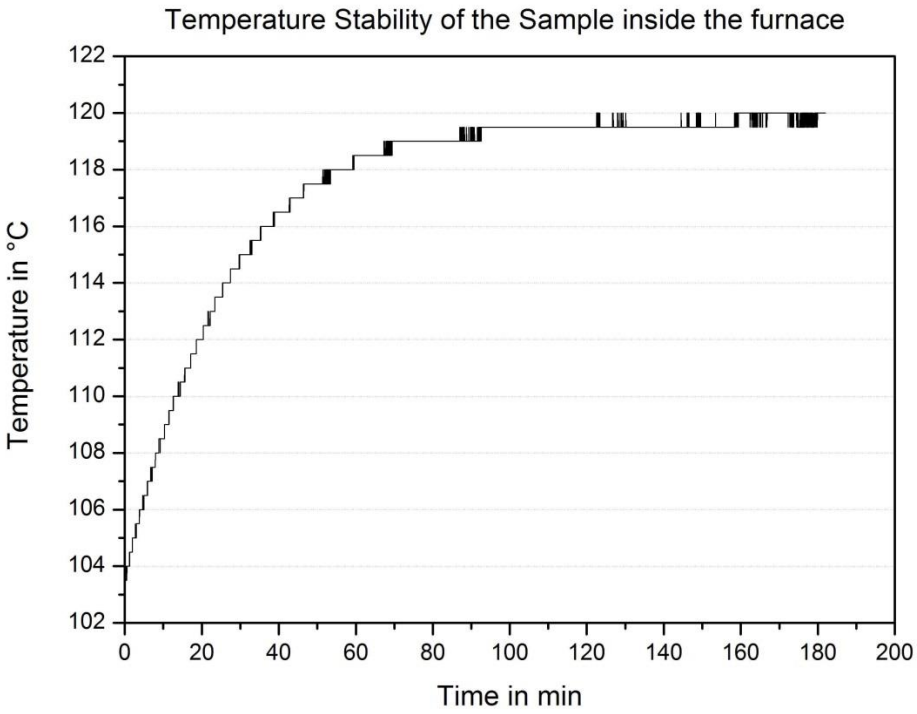

Figure 49 : Temperature stability of the sample measured inside environmental chamber using thermocouple

10.2 Appendix 2

10.2.1 Fractography

10.2.1.1 DHP-UT

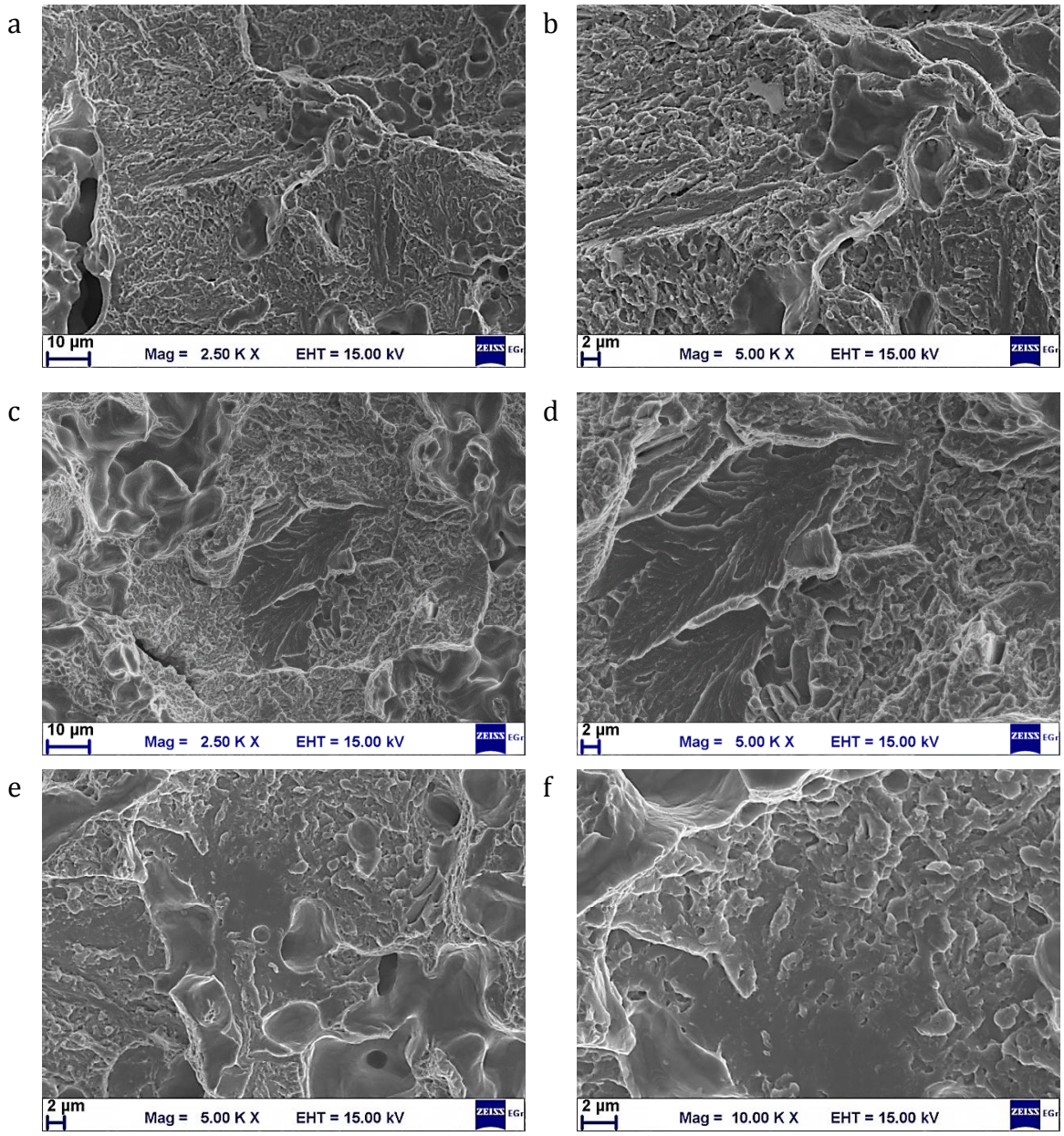

Figure 50

10.2.1.2 DHP-T200

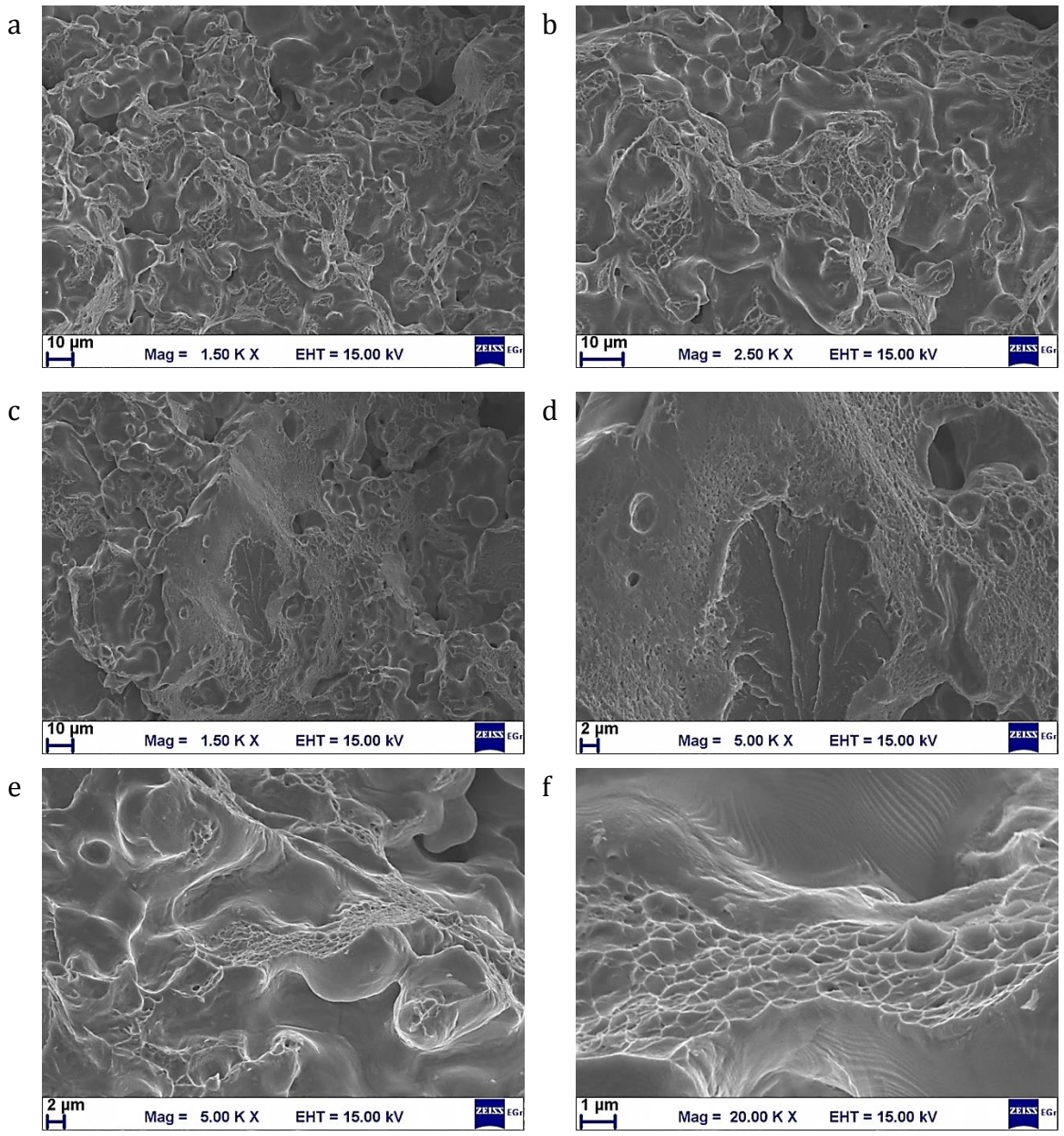

Figure 51

10.2.1.3 DHP-T300

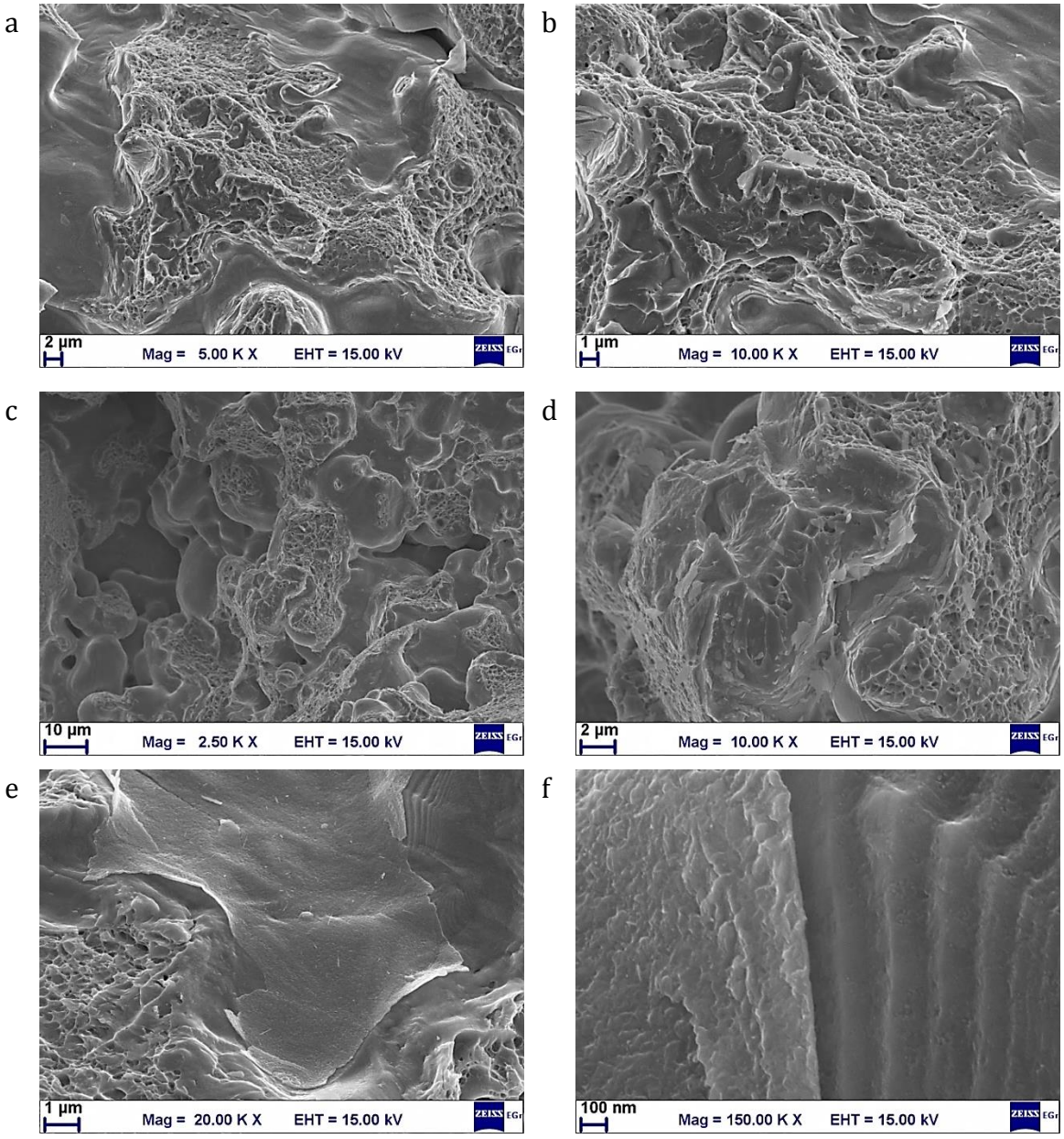

Figure 52

10.2.1.4DHP-DC-UT

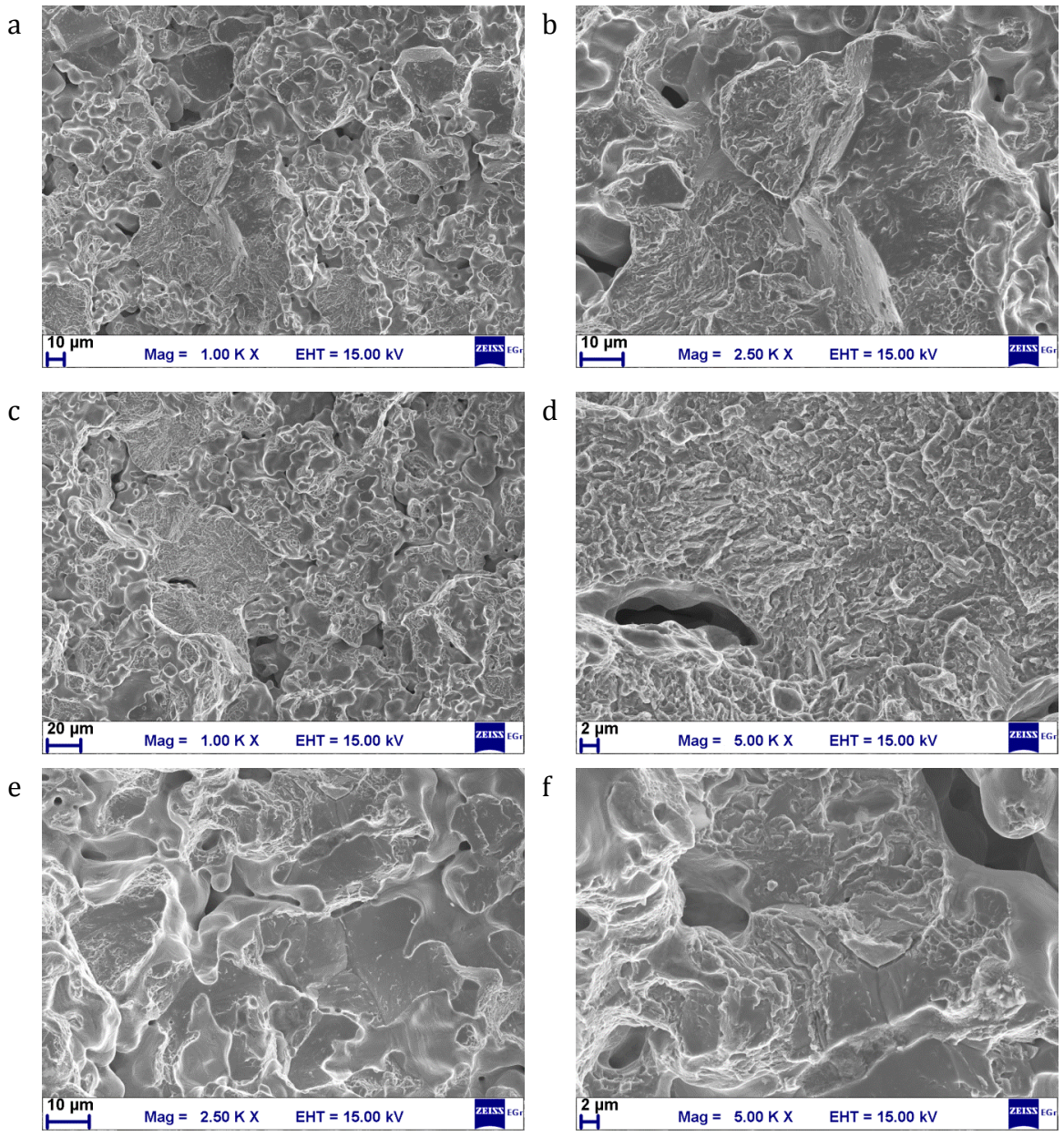

Figure 53

10.2.1.5 DHP-DC-T200

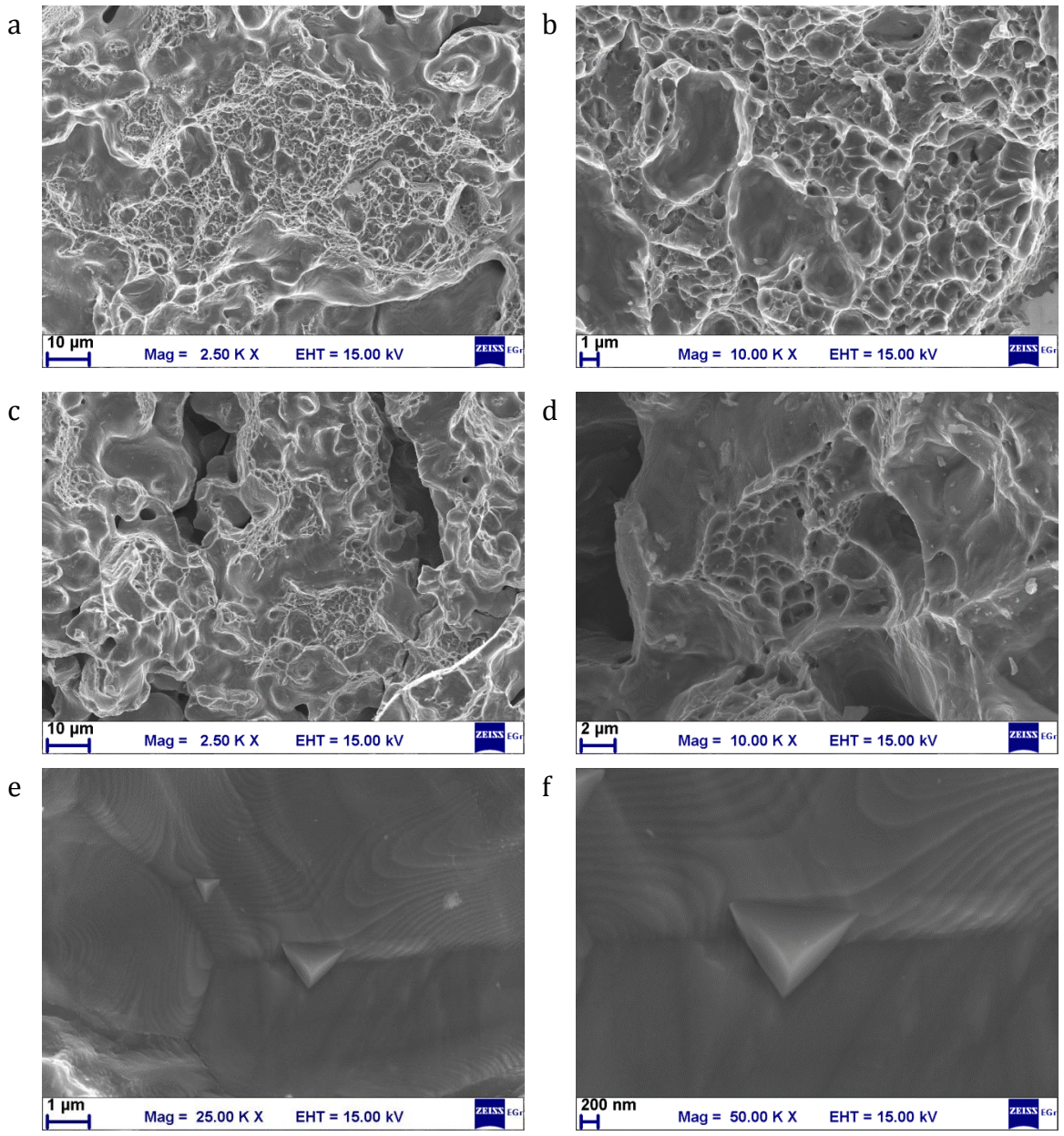

Figure 54

DHP-DC-T300

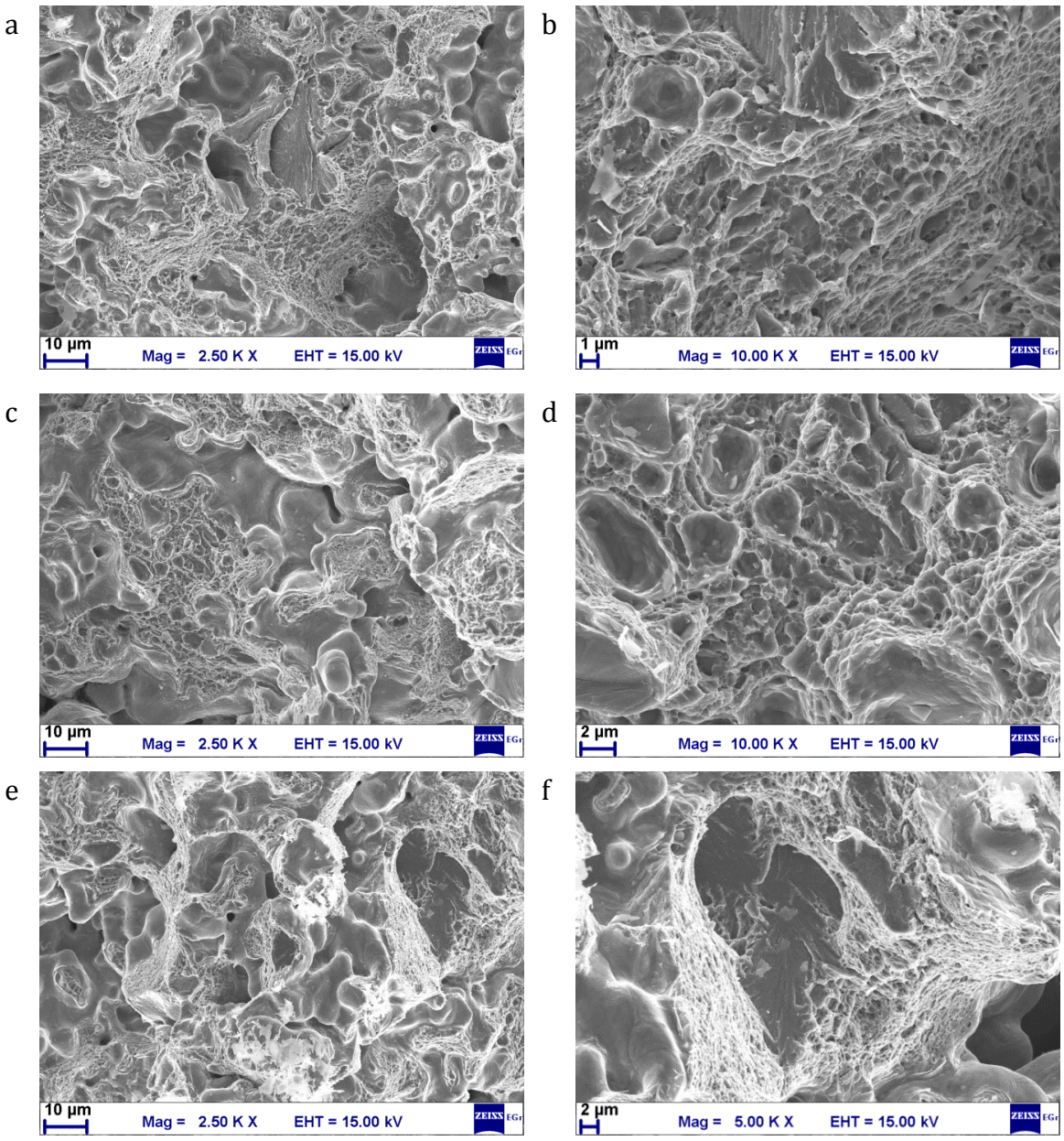

Figure 55

10.3 Appendix 3

10.3.1 Creep Curves

10.3.1.1At different stresses

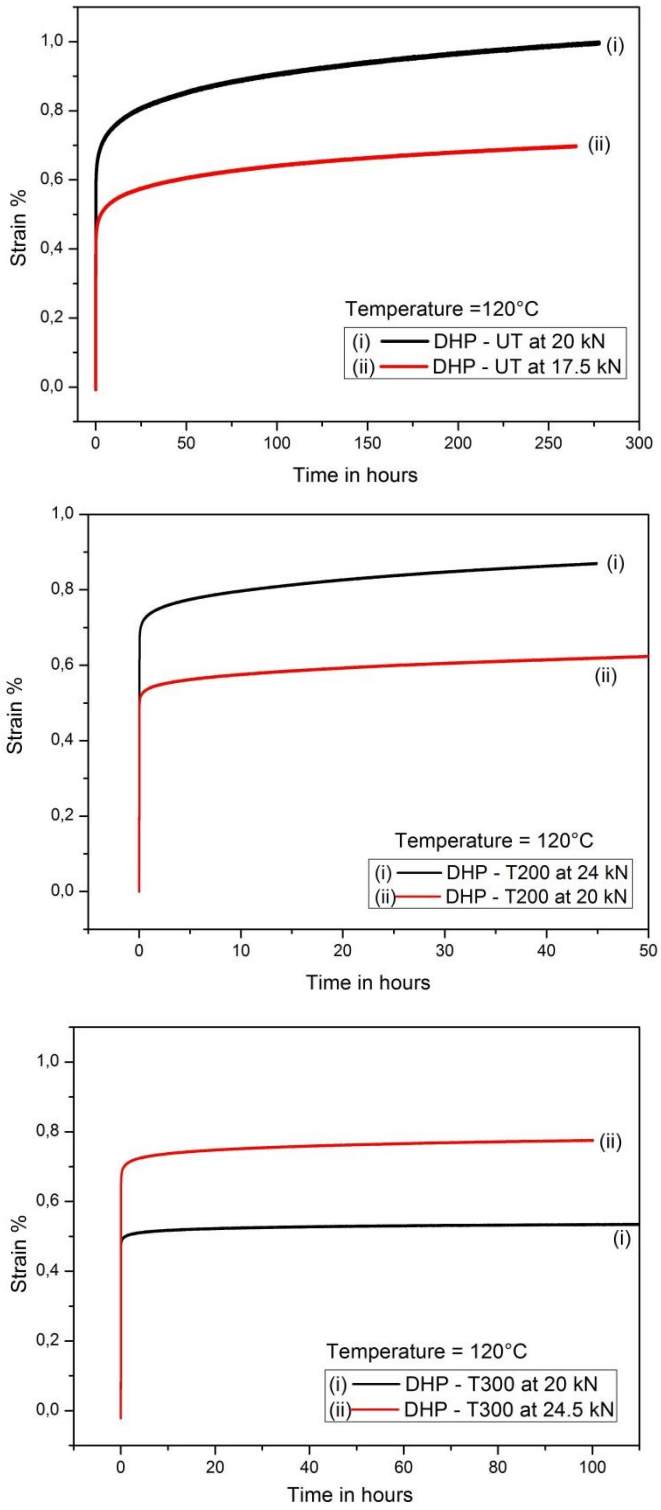

Figure 56

10.3.1.2 At temperature 120°C vs 150°C at constant load of 20 kN

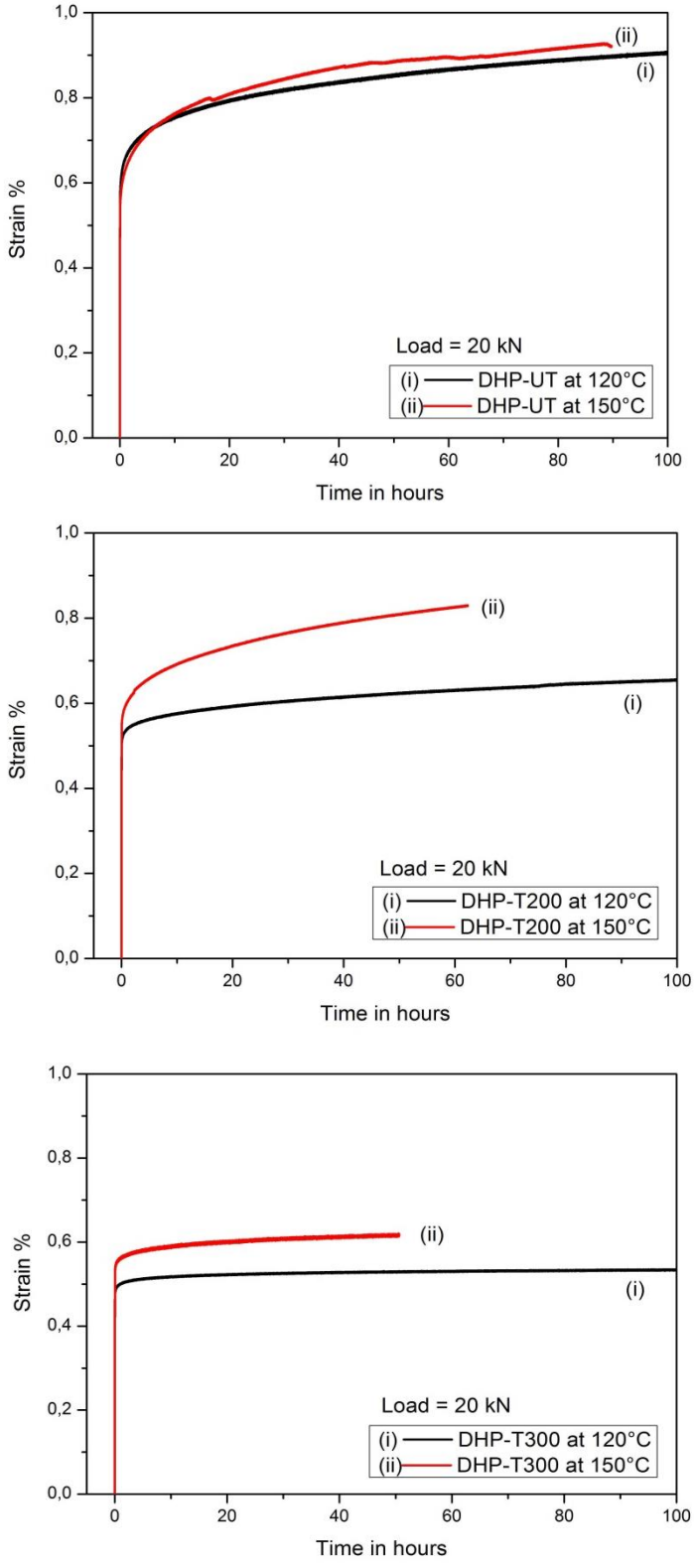

Figure 57